QUANTITATIVE NANO-SURFACE CHEMISTRY

FOR DIABETES SERUM BIOMARKER ASSAYS

By

JINESH NIROULA

Bachelor of Science in Chemistry
Cameron University
Lawton, Oklahoma
2012

Submitted to the Faculty of the
Graduate College of the
Oklahoma State University
in partial fulfillment of
the requirements for
the Degree of
DOCTOR OF PHILOSOPHY
July, 2019

QUANTITATIVE NANO-SURFACE CHEMISTRY

FOR DIABETES SERUM BIOMARKER ASSAYS

Dissertation Approved:

Dr. Sadagopan Krishnan

Dissertation Adviser

Dr. Ziad El Rassi

Dr. Christopher J. Fennell

Dr. Gabriel Cook

Dr. Francisco M. Ochoa Corona

ACKNOWLEDGEMENTS

I would like to express my sincere gratitude and appreciation towards my academic advisor Dr. Sadagopan Krishnan. Without his continuous guidance and support, this dissertation would not have been possible. I would like to thank him for his valuable advice, enthusiasm, and encouragement. I would also like to thank my dissertation committee members Dr. Ziad El Rassi, Dr. Christopher J. Fennell, Dr. Gabriel Cook, and Dr. Francisco M. Ochoa Corona, for their insights and encouragements.

I am grateful towards all our collaborators who made significant contributions in completing the research studies. I am also thankful towards the Department of Chemistry for providing support for the graduate studies. Likewise, I have my deepest regards towards my former and current lab mates who provided valuable discussions, guidance, and encouragements during this path of graduate studies.

I am thankful to all my friends here in the United States who ultimately became my second family. It has been a pleasure walking with you all, enjoying all the ups and downs in life, and treasuring moments of togetherness.

Finally, I am humbly thankful towards my parents (Sovit Bahadur Niroula and Indu Niroula) for their immense support and belief in me. I am grateful towards all of my family members for all the unconditional love and care.

Name: JINESH NIROULA

Date of Degree: JULY, 2019

Title of Study: QUANTITATIVE NANO-SURFACE CHEMISTRY FOR DIABETES SERUM BIOMARKER ASSAYS

Major Field: CHEMISTRY

Abstract: Glucose monitoring devices (e.g., glucometer) are widely established as a successful diabetes management and point-of-care testing systems. However, non-glucose markers such as hormones, autoantibodies, proteins, and other small molecules can provide better assessments for the prediction and management of the disorder and identification of diabetes classes (e.g., type 1 and type 2). The challenges our research community faces in designing an analytical device for such markers are the dynamic range, limit of detection, selective isolation of the analyte, higher background noise due to clinical matrix, and ability to transform the system into a cheap point-of-care device. The main research objective is to design and develop a new diabetes sensor surface chemistry to advance the current analytical capabilities of detecting serum insulin and autoantibodies through novel surface designs.

In this dissertation, I discuss the development of covalent and noncovalent carboxylations of carbon nanotubes for sensitivity enhancement of clinical immunosensors for insulin detection. Additionally, the validation of an electrochemical immunosensor for detection of serum glutamic acid decarboxylase-65 autoantibody through surface plasmon resonance imaging and establishing binding parameters for the antigen-antibody binding are reported. Finally, a low-cost paper-based label-free electrochemical approach is presented for sensitive detection of serum insulin. The dissertation critically discusses the quantitative analytical details of the developed sensors' surfaces.

TABLE OF CONTENTS

Chapter Page

Chapter Page

LIST OF TABLES

Table Page

LIST OF FIGURES

Figure Page

Figure Page

Figure Page

Figure Page

CHAPTER I

IMMUNOSENSOR DESIGNS TO ENABLE CLINICALLY REQUIRED PICOMOLAR DETECTION OF SERUM INSULIN AND AUTOANTIBODIES

1.1 Diabetes pandemic

The growing diabetic disorders and their complications (retinopathy, nephropathy, neuropathy, cardiovascular diseases, and others) are significant health problems and a great economic burden in the United States and globally.[1] "Global report on diabetes" from World Health Organization (WHO) indicated that 422 million adults have diabetes.[2] In the United States, 30.3 million people have diabetes which translates to about 1 in every 10 persons, and accounts for approximately $245 billion on national healthcare costs.[3]

The American Diabetes Association has recently reclassified diabetes into four types: type 1 diabetes (T1D), type 2 diabetes (T2D), gestational diabetes mellitus (GDM), and specific types of diabetes due to other causes such as, diseased pancreas and chemically induced diabetes (Table 1.1).[4] Additionally, there is one more broadly accepted category of diabetes known as latent autoimmune diabetes in adults (LADA). LADA is characterized by slow progression of β-cell failure and presence of autoantibodies against β-cell antigens, however the patient may not require the administration of external insulin for upwards of 6 months after diagnosis.[5]

Table 1.1. Generally accepted classification of diabetes.

Type of diabetes	Characteristic features
Type 1 diabetes (T1D)	Autoimmune β-cell destruction, insulin deficiency
Type 2 diabetes (T2D)	Progressive loss of insulin secretion, insulin resistance
Gestational diabetes mellitus (GDM)	Developed during pregnancy
Specific type of diabetes	Monogenic diabetes syndrome; diseased exocrine pancreas induced; drug/chemical induced
Latent autoimmune diabetes in adults (LADA)	Slow progression of β-cell failure, presence of autoantibodies, does not require insulin administration initially

One of the major achievements in the fight against diabetes was the discovery of insulin in pancreatic extracts of dogs. In 1922, Frederick Banting and Charles Best, with help and guidance from John Macleod discovered insulin and its significance in glucose metabolism and homeostasis.[6] Another major accomplishment in the fight against diabetes was the design and development of the blood glucose sensor.

1.2 State of the insulin sensors and early diabetes markers

1.2.1 Blood glucose sensor

In 1962, Leland C. Clark and Champ Lyons first demonstrated a sensor for measuring glucose concentrations that used glucose oxidase (GOx), an enzyme that converts glucose into gluconic acid, and measured oxygen concentration that was proportional to glucose concentration.[7] Since then, a variety of sensors able to measure glucose concentrations has been demonstrated and perfected such that there is currently a large range of such glucometers in commercial settings. These glucose sensors have been mainly divided into three generations depending on how they communicate with the electrode and generate signals. Almost all of the glucose sensors depend on GOx for enzymatic conversion of glucose into gluconic acid. The first generation of the

glucose sensors used O_2 as the mediator, the second generation incorporated the use of artificial mediators to avoid O_2 deficit conditions, and the third generation worked without employing any mediators.[8,9]

While glucometers are well established as a Point-of-Care (POC) benchmark, the debate about the technical accuracy versus the clinical accuracy of these devices continues.[10] Moreover, glucometers do not provide information relating to difference in the type of diabetes or a person's tendency to develop a clinical onset.

1.2.2 Insulin sensors

Insulin is a 5.8 kDa polypeptide hormone responsible for the glucose homeostasis. It consists of two peptide chains known as A-chain and B-chain linked together with two disulfide bonds, and an additional disulfide bond within A-chain (Figure 1.1). The A-chain consists of 21 amino acids while B-chain has 30 amino acids. Insulin is secreted by the β-cells in the Islets of Langerhans as preproinsulin which consists of the two peptide chains, a C-peptide region, and an additional 24-residue signal peptide.[11] This precursor cleaves off to become proinsulin which again cleaves off into insulin and C-peptide.

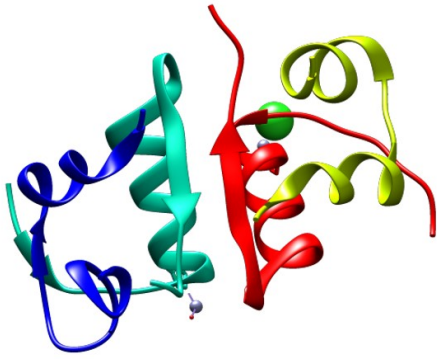

Figure 1.1. Structure of human insulin [PDB ID: 4F1A].

Detecting insulin in biological fluids can provide critical information that can help in the course of diabetes treatment. However, unlike millimolar glucose, insulin is present at very low concentrations (picomolar) in human blood. In clinical settings, fasting blood sugar level less than 100 mg dL^{-1} (< 5.6 mM) is normal, 100-125 mg dL^{-1} (5.6 – 6.9 mM) is considered prediabetes, and 126 mg dL^{-1} or higher (> 7 mM) indicates diabetes.[12] The fasting blood insulin concentrations under normal conditions is ~ 50 pM, and < 50 pM and > 70 pM indicates onsets of type 1 and type 2 diabetes respectively.[13- 16] Due to this ultra-low concentration, designing analytical sensor that is sensitive, selective, robust, and reproducible for such non-glucose biomarkers is challenging.

Previous research from our laboratory demonstrated unique surface design strategies for measuring insulin in biofluids. Our group reported the first electrochemical mass sensor that detected serum insulin conjugated to magnetic particles and captured via antibodies immobilized on thiol modified gold coated quartz resonators.[17] The magnetic particles-insulin conjugation chemistry was later extended to design a voltammetric sensor on a pyrolytic graphite electrode modified with multiwall carbon nanotubes and 1-pyrenebutyric acid assembly.[18] The carbon nanostructure immunoassembly allowed a detection limit of 5 pM of insulin in 50% human serum. Additionally, the serum matrix effect on the detection signal was studied on a surface plasmon resonance imager (SPRi) platform by monitoring serum insulin dilution captured by magnetic nanoparticles.[19] Two times diluted serum insulin conjugated to magnetic particles exhibited higher SPRi signals achieving detection limit of 5 pM, when compared to other serum dilutions. In another work, SPRi was used to detect two biomarkers in one chip, insulin and glycated hemoglobin (HbA1c), in 20-times diluted whole blood.[20] Magnetite nanoparticles decorated with quantum dots were used for covalent immobilization of aptamers for selective isolation and capturing of insulin and HbA1c in the diluted whole blood samples. The detection limits for insulin and HbA1c were 4 pM and 1% respectively.

Recently, Li *et al.* demonstrated an Orange II (water soluble electroactive dye) and Au nanoparticles composites on a graphene modified glassy carbon electrode to measure insulin concentration using differential pulse voltammetry.[21] The method allowed to achieve an impressive linear range of 10 fM – 500 pM with a detection limit of 6 fM.

Yagati *et al.* demonstrated a reduced graphene oxide modified interdigitated chain electrode for label free detection of insulin concentrations prepared in buffer solution.[22] A change in the relative capacitance was monitored as the detection signal for increasing insulin concentrations. Another report by Tabrizi *et al.* employed differential pulse voltammetry to detect insulin molecules on screen printed electrodes modified with ordered mesoporous carbon that was chemically modified with 1,3,4,8-pyrenetetrasulfonate to immobilize insulin aptamers.[23] Using methylene blue as the redox probe, a linear range of 1.0 fM – 10.0 pM and detection limit of 0.18 fM was achieved.

This dissertation explores strategies for enhancing immunosensing techniques applicable to diabetes biomarkers using covalent and noncovalent carboxylations of carbon nanotubes, and plasmonic property of graphene. Additionally, a low-cost electrochemical approach for sensitive detection of serum insulin molecules is reported.

1.2.3 Autoantibodies in T1D

T1D is an autoimmune disease categorized by the destruction of pancreatic β-cells that has been related to genetic, environmental, and metabolic factors. The destruction of β-cells leads to insufficient production of insulin that eventually results in hyperglycemia. Studies have reported that autoimmunity occurs years earlier than the clinical onset of T1D. This phase is also characterized by the presence of autoantibodies against β-cell antigens namely: glutamic acid decarboxylase 65 (GAD65), tyrosine phosphatase-related islet antigen 2 (IA-2), insulin, transglutaminase, and zinc transporter-8.[24] Nearly all T1D patients have at least one of these

autoantibodies. Additionally, adults testing positive for two or more autoantibodies have ~77% chance of developing T1D in the next five years. As per a study, 43.5% of children who tested positive for two or more autoantibodies developed T1D within 5 years, 69.7% of them within 10 years, and 84.2% within 15 years.[25] These statistics highlight the importance of detecting the aforementioned biomarkers in clinical matrices.

In 1995, Falorni *et al.* reported a radioimmunoassay for detection of GAD-65 autoantibodies using ^{35}S or ^{3}H recombinant human ligands.[26] Few years later, Walikonis *et al.* reported a radioimmunoassay for the detection of the same biomolecule using ^{125}I as labels.[27] Zhang *et al.* reported a plasmonic chip for detecting autoantibodies for T1D using IRDye800-labeled anti-human IgG antibodies and studying fluorescence spectroscopy.[28] While their assay time was less than 2 hours, the multiple surface modifications took more than 12 hours and required a microarray printing robot and incorporation of expensive fluorescence labels. In addition, the study required complicated data manipulations. Zhao *et al.* developed an electrochemiluminescence assay for multiplexed detection of four autoantibodies.[29] However, their double antigen assay required multiple labels including sulfo- and linker-tagged antigens with overall incubations time surpassing 24 hours. 3-Screen islet cell autoantibody enzyme-linked immunosorbent assay (ELISA) reported by Amoroso *et al.* also employed double antigen technique with multiple labels and incubation time surpassing 24 hours.[30]

1.3 Limitations and need for new sensors with simplicity and sensitivity for real samples

While there have been unique sensor designs exhibited for diabetic biomarkers, they all lack in area of simplicity by requiring complicated surface designs. Additionally, most of the aforementioned sensors detect biomarkers in buffer solution. This results in uncertain outcomes when the sensing technique is translated to biological samples. Increase in background signal, decrease in dynamic range, and higher limit of detections are some of the limitations encountered

when biological samples are involved. Moreover, the assay time tends to require long hours as well as high-end instruments with expensive labels. Additionally, translating the biosensor into a point-of-care testing (POCT) system, which is encouraged by NIH, also becomes tricky.

1.4 Significance of electrochemical sensors

Electrochemical methods are the basis of modern biosensing techniques as they provide a relatively cheaper alternative to expensive laboratory instruments in a clinical setting. Electrochemical biosensors provide the platform for converting a biological event into an electronic signal thus allowing the analysis of the biological environment. A typical electrochemical cell is composed of a working electrode (WE), reference electrode (RE), and counter electrode (CE).

Detection of biomarkers can be performed via several techniques including, but not limited to, radioimmunoassay, enzyme-linked immunosorbent assay (ELISA), liquid chromatography, electrochemical, and optical methods. Among these, electrochemical methods are widely popular as they do not require radioactive labels or sophisticated instruments, but a benchtop potentiostat only. Furthermore, an electrochemical sensor can potentially be transferred into a POCT system.

1.4.1 Amperometry

Amperometry is an electrochemical method that continuously measures current resulting from the redox process of an electroactive species at the WE at an applied constant potential (Figure 1.2). The current is proportional to the bulk concentration of the electroactive species in the sample.

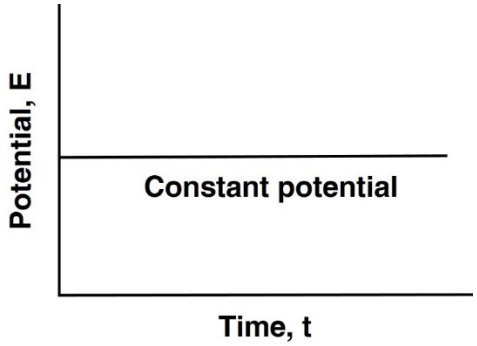

Figure 1.2. Constant potential waveform for amperometric techniques.

Using flow-injection amperometry, we designed an immunosensor for insulin detection in 20-fold diluted human serum (Figure 1.3). π-π stacking of 1-pyenebutyric acid over dry-coated carboxylated multiwall carbon nanotubes increased the number of biomolecule immobilization sites thereby, increasing the number of immobilized capture molecules for insulin detection. The current signals were proportional to the amount of insulin bound to the sensor surface (Figure 1.3-B).

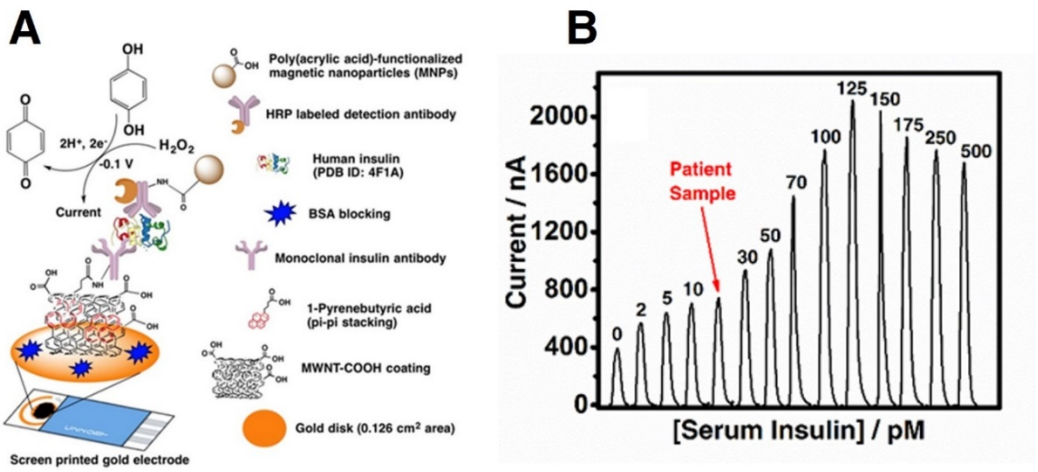

Figure 1.3. (A) Amperometric immunosensor for insulin detection 20-fold diluted in human serum. **(B)** Current signals corresponding to different of insulin concentrations bound to the sensor surface with a representative patient sample analysis. Reproduced from Niroula, J.; Premaratne, G.; Ali Shojaee, S.; Lucca, D. A.; Krishnan, S. *Chem. Commun.* **2016**, *52*, 13039-13042 with permission from the Royal Society of Chemistry.

1.4.2 Electrochemical impedance spectroscopy (EIS)

Electrochemical impedance is the measure of the ability of a circuit to resist the flow of electric current and is usually measured by applying an AC potential to an electrochemical cell and measuring the current. Generally, a sinusoidal potential excitation is applied which results in an AC current signal. This current signal will be sinusoidal at the same frequency but is shifted in phase (ϕ). If an excitation signal, E_t, results in the response signal, I_t, the electrochemical impedance (Z) is expressed as shown below.

$$Z = \frac{E_t}{I_t} = \frac{E_0 \sin(\omega t)}{I_0 \sin(\omega t + \phi)} = Z_0 \frac{\sin(\omega t)}{\sin(\omega t + \phi)} \qquad \text{(Equation 1.1)}$$

Here, E_t is potential at time t, E_0 is amplitude of the signal, ω is the radial frequency, I_t is response signal, I_0 amplitude of signal, and Z_0 is the impedance magnitude. EIS can also be represented as a complex number, $Z = Z_{re} + jZ_{im}$, where Z_{re} denotes real impedance and Z_{im} denotes imaginary impedance.

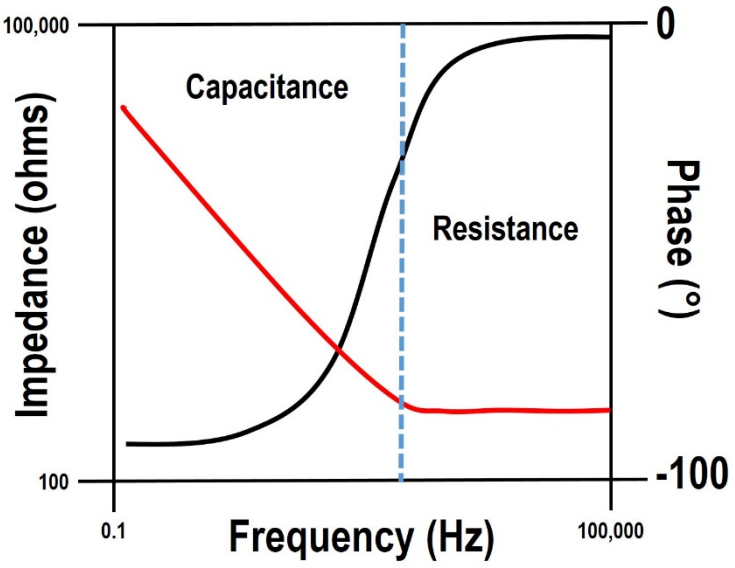

Figure 1.4. Bode plot representing capacitance and resistance region of a sensor.

In the presence of a redox probe, a faradaic process occurs where resistance of the electrolyte solution, R_s, Warburg impedance, Z_W, double layer capacitance, C_{dl}, and electron transfer resistance, R_{et}, all contribute to the interfacial electronic circuit. However, in the case of a label-free approach, only non-faradaic impedance comes into play. Here, the Z_W and R_{et} tends to infinity and only the C_{dl}, which depends on the dielectric permittivity of the surface molecules becomes the variable unit.[31] This non-faradaic behavior is demonstrated by the Bode plot (Figure 1.4). At higher frequencies, the sensor behaves more as a resistor and the impedance remains constant. However, while scanning at lower frequencies, where the phase angle is closer to -90°, the sensor behaves significantly as a capacitor.[32] Unlike faradaic processes and ELISA, non-faradaic EIS is label-free technique.

Using this concept, we designed a paper-based strategy to detect insulin molecules spiked in 10% human serum (Figure 1.5). The C_{dl} becomes the $C_{interface}$ representing the interfacial capacitance. While resistance dominates at higher frequencies, the sensor behaves as capacitor at lower frequencies. The relative change in capacitance was monitored at 10 Hz frequency for increasing concentrations of serum insulin. In this study, carboxylated graphene was chosen for its aqueous dispersibility and superior biocompatibility. Additionally, the designed sensor was validated using amperometric technique.

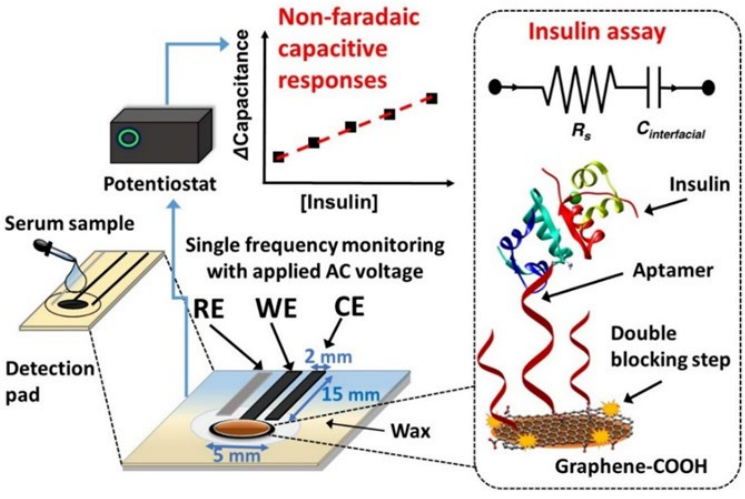

Figure 1.5. Design of the paper-based capacitive sensor for monitoring insulin concentrations in 10% human serum.

1.5 Independent validation with surface plasmon resonance imaging (SPRi)

In another study, we used SPRi as a validation method of an electrochemical detection technique based on faradaic-EIS for glutamic acid decarboxylase-65 (GAD-65) autoantibodies detection in human serum. Carboxylated graphene was used to immobilize GAD-65 antigen as the biorecognition element, which captured autoantibodies from serum samples. This study allowed to establish optimal conditions and obtain binding parameters for the GAD-65 antigen-antibody interactions.

Surface plasmon resonance (SPR) is a label-free optical detection method that has gained significance in the analysis of biomolecular interactions. SPR refers to the collective oscillations of the conduction electrons in noble metals (usually thin films of gold). Surface plasmons (SPs) are electromagnetic waves that are excited by p-polarized light and propagate parallel to the surface while decaying exponentially away from the surface. The maximum decay length of a SP is ~ 200 nm, and SPR is used to monitor changes in the index of refraction caused by changes in thickness of the molecular layer above the gold surface within this length.[33] SPR allows real-time monitoring of biomolecular interactions as well as provides binding kinetics and affinity information regarding the same.[34]

In SPRi, both the incident angle and wavelength are fixed while a CCD camera monitors the reflected light in an array format (GWC Technologies, Inc). Initially, the SPR angle is adjusted and then the biomolecular interactions are monitored upon changes in the intensity of reflected light in an array format (Figure 1.6). The SPR angle is the angle of incidence where the reflected intensity is at minimum due to maximum generation of SPs. The array format allows multiple measurement of biomolecular interactions at the same time.

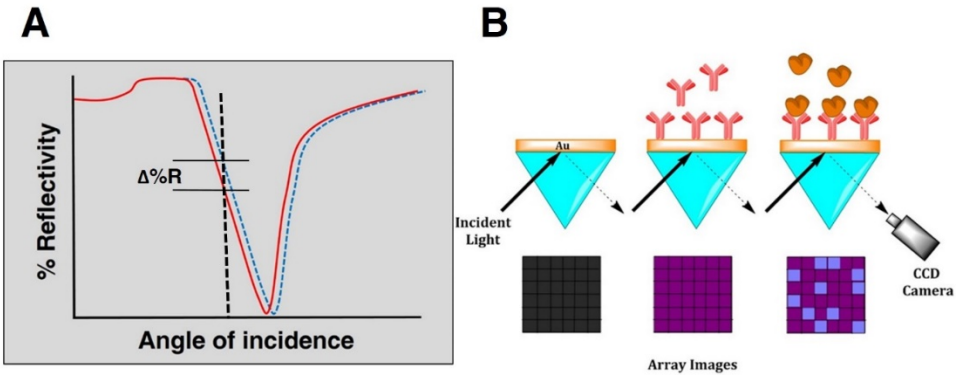

Figure 1.6. (A) Measurement of reflectivity as a function of incident angle. Initially, an SPR angle is determined (red curve) and after molecules adsorb to the surface the angle shifts to higher angle (blue curve.) SPRi monitors change in reflectivity (Δ%R) based at a fixed angle (dashed-black-line). **(B)** The SPRi intensity of reflectivity increases with increasing biomolecular interactions at the gold surface.

1.6 Rationale and novelty of approaches derived in this dissertation research

The sensitivity of an immunosensor mostly depends on analyte loading which in turn depends on availability of biorecognition sites. In Chapter II, we demonstrate a novel approach for increasing the number of immobilization sites for biorecognition elements (insulin antibodies in this case) by π-π stacking 1-pyrenebutyric acid on basal sidewalls of carboxylated multiwall carbon nanotubes. The strategy of combining covalent and non-covalent carboxylations of carbon nanotubes increases the number of carboxyl groups on sensor surface by approximately 4.5 times when compared to carboxylated nanotubes only. This in turn allowed ~ 3 times more antibody immobilization on the sensor surface.

Chapter III presents a SPR immunoarray validation for GAD-65 antigen-antibody interaction. Graphene as a novel 2D nanostructure is utilized to enhance the SPRi signals for antigen antibody interactions. Raman spectroscopy demonstrated that graphene on gold

composites enhances plasmonic properties by ~ 5.5 times. Additionally, binding parameters for the antigen-antibody interactions were also established.

Finally, Chapter IV reports the first paper-based label-free detection of serum insulin. This study provides the initial assessment to shift towards label-free detection of biomolecules in biological matrices. The designed paper-based detection facilitates a low-cost methods of analyte detection.

1.7 Significance of results obtained

The results obtained in this dissertation enabled the detection of picomolar concentrations of serum insulin without using complicated surface designs. In principle, the designed sensor surfaces can be adapted to detect any biomolecule or small molecule of interest. We also report a paper-based method for label-free detection of serum insulin using non-faradaic EIS. This has allowed us to focus towards multiplexing on paper-based surface for other diabetes markers. ELISA correlations using patient samples demonstrated the applicability of the designed sensors in clinical setting.

Using SPR immunoarray, we validated the electrochemical array for detection of GAD-65 autoantibody as well as presented the binding constant for the antigen-antibody interactions. The binding parameters can be used as a standard reference for monitoring GAD-65 antigen-antibody interaction in other detection approaches. Additionally, the inclusion of graphene exhibited a plasmon enhancing property as well as lowered background signals.

These studies do have clear limitations. For example, achieving a wider dynamic range with lower limits of detection in undiluted biological matrices would have been ideal. Nevertheless, the dissertation demonstrates novel sensor surface designs with quantitative details on the surface carboxyl groups and protein loading which surpasses traditional limitations.

1.8 Summary

The ultrasensitive detection of diabetes biomarkers can enable an optimized management of the disorder and potentially provide a prediction model for the onset of the disease. This dissertation demonstrates the surface chemistry for sensitive detection of serum insulin in clinically relevant range. Additionally, a validation of SPR immunoarray is presented for detection of autoantibodies in serum matrix. The surface chemistry developed is useful for detection of any other biomolecules using relevant antigen-antibody complexes. The future direction encompasses multiplexing diabetes biomarkers in a paper-based platform in undiluted biological matrix for point-of-care testing.

CHAPTER II

COVALENT AND NONCOVALENT CARBOXYLATIONS OF CARBON NANOTUBES FOR SENSITIVITY ENHANCEMENT OF CLINICAL IMMNUOSENSORS

2.1 Introduction

The large conductive surface area of carbon nanotubes along with ease of functionalization has allowed the development of highly sensitive electrochemical immunosensors and electrodes featuring chemical or enzymatic catalysts yielding high electrocatalytic currents.[35-42] Conventional covalent carboxylation (e.g., by acid treatment, amidation, thiolation) and recently developed noncovalent carboxylation of carbon nanotubes (e.g., π-π interactions, DNA wrapping) have a remarkable significance in the multiple areas of electronics, biosensors, engineering, materials science, fuel cells, and renewable energy.[43-49] Additionally, new functionalization strategies of carbon nanotubes to obtain a fundamental understanding of its structure in enzyme biosensors and electrocatalysis are still evolving.[50-52]

This study describes the π-π stacking of 1-pyrenebutyric acid (Py-COOH) with carboxylated multiwall carbon nanotubes (MWNT-COOH) on gold screen printed electrodes (AuSPEs) for covalent immobilization of monoclonal insulin antibody ($Ab_{surface}$) and detection of insulin spiked in 5% serum. To minimize the serum matrix effect and amplify the current signal,

Adapted from Niroula, J.; Premaratne, G.; Ali Shojaee, S.; Lucca, D. A.; Krishnan, S. *Chem. Commun.* **2016**, *52*, 13039-13042 with permission from the Royal Society of Chemistry.

we captured insulin present in serum by horseradish peroxidase (HPR)-labeled second insulin antibody (detection antibody) attached to magnetite (Fe_3O_4, 1 mg contains ~ 1.8 x 10^{12} particles) nanoparticles. Using nanoparticles labeled with insulin antibodies allows easy isolation of insulin molecules from serum matrix. This study reports the effect of combining covalent and noncovalent carboxylations of MWNTs for developing highly sensitive serum insulin amperometric immunosensors. The application of this methodology to other enzyme-catalyzed reactions seeking sensing and electrocatalysis adds an immense significance to the findings in this report.

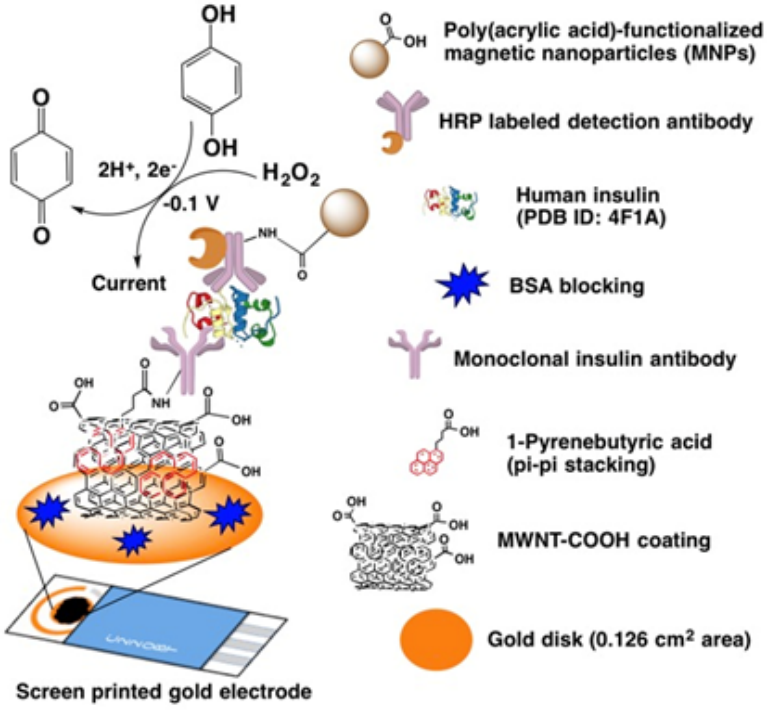

Figure 2.1. Schematic representation of the designed serum insulin immunosensor.

Figure 2.1 shows the amperometric insulin immunosensor designed in this study for measuring insulin levels in human serum. The detailed experimental procedure for construction of the immunosensor under optimized conditions is provided in the experimental section. In brief, an AuSPE was dry coated with MWNT-COOH. Py-COOH was then π-π stacked onto the basal plane sidewalls of the MWNT-COOH surface.[35,53,54] Following this, the surface carboxyl groups

were activated by treating with a freshly prepared solution of 1-ethyl-3-(3-(dimethylamino)propyl)-carbodiimide (EDC, 0.4 M) and N-hydroxysuccinimide (NHS, 0.1 M) mixture in deionized water to convert them into N-succinimidyl esters for covalent attachment with the lysine residues of $Ab_{surface}$ (amine-carboxylic acid coupling chemistry to form amide bonds).[54] The surface was then blocked with bovine serum albumin (2% BSA) to minimize nonspecific binding.[55] The sensor was incubated with serum insulin conjugates prepared by capturing insulin from serum using poly(acrylic acid)-functionalized magnetite nanoparticles (MNPs) that are covalently attached with HRP-labeled rabbit polyclonal anti-insulin antibody (Ab_{HRP}). The resulting serum insulin conjugate is denoted as MNP-Ab_{HRP}-insulin (Figure 2.1).

Amperometric signals were monitored for the binding of MNP-Ab_{HRP}-insulin conjugates onto $Ab_{surface}$ at an applied constant potential of – 0.1 V vs. a pseudo Ag reference electrode. All procedures were completed off-line except the detection step. For detection, a solution containing 1 mM hydroquinone (HQ) mediator and 0.5 mM H_2O_2 in phosphate buffered saline (PBS, 10mM), pH 7.4 was delivered onto the sensor surface via a syringe pump at a flow rate of 200 μL min^{-1}. The HRP-label (present in the MNP-Ab_{HRP}-insulin conjugate) catalyzed oxidation of HQ to benzoquinone in the presence of H_2O_2 was monitored as current signals, which are proportional to the concentration of serum insulin bound on the AuSPE sensor surface (Figure 2.1). The MNP-Ab_{HRP} strategy offers the isolation of insulin from complex serum by simple use of a small magnet, improved antibody-antigen binding selectivity, increased signals from large antibody-insulin complexes carrying MNPs and minimized interferences of signals from the free serum matrix.[17,56]

Figure 2.2 shows the experimental setup of the immunosensor for serum insulin detection. Once the immunosensor electrode was connected to a 3-electrode configuration in a microfluidic channel, a constant –0.1 V potential was applied. A syringe pump was used to deliver 1 mM HQ and 0.5 mM H_2O_2 containing PBS solution over the serum insulin-bound

sensor surface. Corresponding amperometric signals were recorded by a computer connected with a potentiostat.

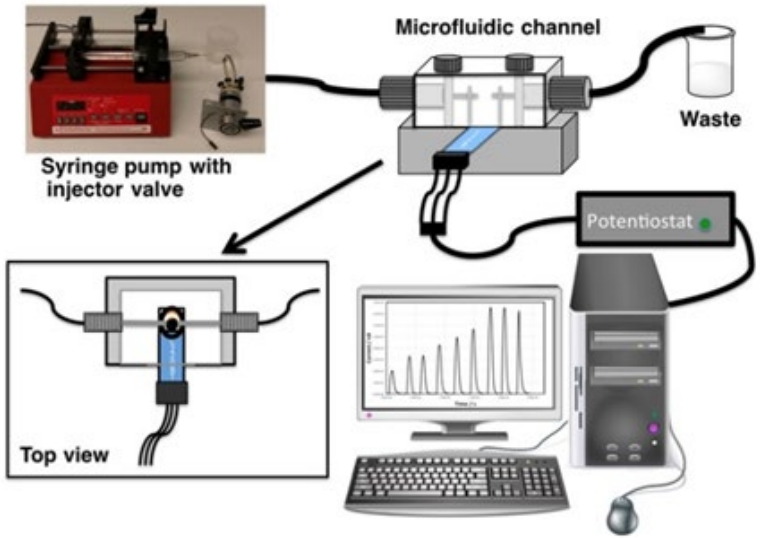

Figure 2.2. Experimental setup of the designed immunosensor. The top view of the microfluidic channel is shown on the bottom-left corner.

2.2 Experimental

2.2.1 Reagents and materials

Screen-printed gold electrodes (AuSPEs, DRP-C220BT, 0.126 cm^2 Au geometric area, DropSens Inc.) were obtained from Metrohm USA, Inc. (Riverview, FL). Carboxylic acid-functionalized multiwalled carbon nanotubes (MWNT-COOH), 1-ethyl-3-(3-(dimethylamino)propyl)-carbodiimide (EDC), *N*-hydroxysuccinimide (NHS), mouse monoclonal anti-insulin antibody ($Ab_{surface}$), bovine serum albumin (BSA, ≥ 98% purity), hydrogen peroxide solution (H_2O_2), and hydroquinone (HQ) were purchased from Sigma-Aldrich (St. Louis, MO). 1-Pyrenebutyric acid (Py-COOH) and the NanoOrange Protein Quantitation Kit were purchased from Thermo Fisher Scientific (Waltham, MA). Recombinant human insulin (> 99%) from yeast was purchased from Kerafast, Inc. (Boston, MA). Horseradish peroxidase (HRP)-labeled rabbit polyclonal anti-insulin antibody (Ab_{HRP}) was purchased from LifeSpan BioSciences, Inc. (Seattle, WA). Poly(acrylic

acid)-functionalized magnetic nanoparticles (MNPs, fluidMAG-PAS, 100 nm hydrodynamic diameter, 1 mg contains ~1.8 x 10^{12} number of particles) was obtained from Chemicell GmbH (Berlin, Germany). A T2D patient serum sample was sourced from BioreclamationIVT (Westbury, NY). Thionyl chloride was purchased from TCI America (Portland, OR). 4-nitrophenol (97%), 1,4-dioxane (99+%), and trimethylamine (99%) were obtained from Alfa Aesar (Ward Hill, MA).

2.2.2 Apparatus and instrumentation

The surface morphology of the insulin immunosensor was imaged using scanning electron microscopy (SEM, Model: JEOL JXM 6400). To characterize the stepwise surface modification of the immunosensor on the electrode, a Nicolet iS50 Fourier transform infrared spectrometer (FTIR, Thermo Scientific) and a WITec alpha-300 confocal Raman microscope (WITec GmbH, Ulm, Germany) were used. Amperometric responses were recorded using a CHI 6017E electrochemical analyzer (CH Instruments, Austin, TX). All electrochemical studies were conducted in phosphate buffered saline (PBS, pH 7.4, 10 mM phosphate, 0.14 M NaCl, 2.7 mM KCl) at room temperature (23 ^{o}C). Cyclic voltammetric quantitation of surface -COOH groups was performed with a CHI 6017E electrochemical workstation in phosphate buffer (pH 6.8). Fluorescence measurements for $Ab_{surface}$ quantitation was carried out using a Cary Eclipse Fluorescence Spectrophotometer (Agilent Technologies, Santa Clara, CA).

2.2.3 Preparation of the insulin detection antibody-magnetic nanoparticles conjugate (MNP-Ab_{HRP}-insulin)

The conjugates were prepared using the protocol provided by the manufacturer (Chemicell GmbH). Briefly, 150 µL of a freshly prepared aqueous solution of 0.4 M EDC and 0.1 M NHS was added to 68 µL of MNPs (25 mg/mL, i.e., 1.7 mg) and gently rotated for 10 minutes to activate the poly(acrylic acid) –COOH groups of MNPs. The activated MNPs were separated

using a small cleaved magnet (this provides better surface roughness than a smooth magnetic surface) within 15 s and the supernatant consisting of the unreacted EDC/NHS solution was removed. The MNPs were washed twice with 150 µL of PBS. Then, 20 µL of HRP labeled anti-insulin antibody (0.42 mg/mL) in 250 µL of PBS buffer was added to the activated MNPs and the mixture was rotated gently for 1 hour at room temperature. The obtained MNP-Ab_{HRP} was washed three times with 0.1% BSA in PBS (PBS-BSA). The washed MNP-Ab_{HRP} was divided equally into six aliquots. To each aliquot, 140 µL of different insulin concentrations spiked in 5% human serum was added and gently rotated for 1 hour. Thus obtained, MNP-Ab_{HRP}-insulin conjugates were washed three times with PBS-BSA. The conjugates were then suspended in 140 µL PBS giving a final concentration of 2 mg/mL MNPs in the prepared conjugates, an optimal concentration that provided good reproducibility in the sensor. Similar protocol was used to prepare bioconjugates for a T2D patient's serum sample by diluting it 20-times in PBS to obtain 5% serum containing insulin.

2.2.4 Preparation of immunosensor electrodes

AuSPEs were cleaned by washing them in ethanol and then with water. A 3.5 µL suspension of MWNT-COOH (2 mg/mL) in dimethylformamide (DMF) was added to each AuSPE surface and dried at room temperature. Then 7 µL of 1-pyrenebutyric acid (Py-COOH, 10 mM) in DMF was added to each AuSPE and incubated for 1 hour in a closed moisturized environment to avoid drying of the Py-COOH solution. This allowed the formation of strong π-π stacked MWNT-COOH/Py-COOH complexes on the AuSPEs. The electrodes were rinsed well with water. All further modifications on the electrodes were done at 4 ˚C. To the MWNT-COOH/Py-COOH modified electrodes, 10 µL of an aqueous solution containing the mixture of 0.4 M EDC and 0.1 M NHS was added (per electrode) to activate the surface carboxylic acid groups for a duration of 10 min. The electrodes were rinsed with PBS and a 10 µL solution of 100 µg/mL monoclonal anti-insulin antibody ($Ab_{surface}$) in PBS was added to each electrode and incubated for 1 hour. This

allowed for the amine-carboxylic acid coupling reaction and formation of the covalently attached $Ab_{surface}$ via amide bonds onto the MWNT-COOH/Py-COOH modified AuSPEs. The electrodes were then rinsed with PBS, and the surface was blocked for minimizing nonspecific binding by adding 10 μL of 2% BSA in PBS and incubating for 30 minutes. The electrodes were then rinsed with PBS again. Finally, 10 μL of MNP-Ab_{HRP}-insulin conjugates prepared with various serum insulin concentrations were placed on the electrodes and incubated for 1 hour. The electrodes were rinsed in PBS and were fitted into a microfluidic channel to measure amperometric responses at an applied constant potential of -0.1 V vs pseudo Ag while delivering PBS containing 1 mM HQ and 0.5 mM H_2O_2 over the immunosensor surface at a flow rate of 200 μL min^{-1}. Similar to the described MWNT-COOH/Py-COOH/$Ab_{surface}$/ BSA immunosensor, we designed a sensor without the π-π stacking of Py-COOH (i.e., MWNT-COOH/ $Ab_{surface}$/BSA on AuSPEs) for serum insulin measurements using the MNP-Ab_{HRP}-insulin conjugation strategy for comparative measurements.

2.3 Results and discussion

2.3.1 Immunosensor optimization and characterization

The scanning electron microscopy (SEM) image of bare AuSPEs (Figure 2.3-A) shows the characteristic roughness that would be expected for the purchased rough gold surface SPEs manufactured by curing gold ink over a ceramic substrate at low temperature (DropSens Inc.). Dry-coating MWNT-COOH onto AuSPEs resulted in cylindrical tubular structures of the nanotubes (Figure 2.3-B). Further modifications of the electrode with π-π stacked Py-COOH, covalently attached $Ab_{surface}$, and BSA blocking respectively changed the tubular structures to become thicker and denser (Figures 2.3-C, D, and E). After the selective binding of the MNP-Ab_{HRP}-insulin conjugate onto $Ab_{surface}$, the presence of the nanoparticles bound on the sensor surface was observed (Figure 2.3-F).

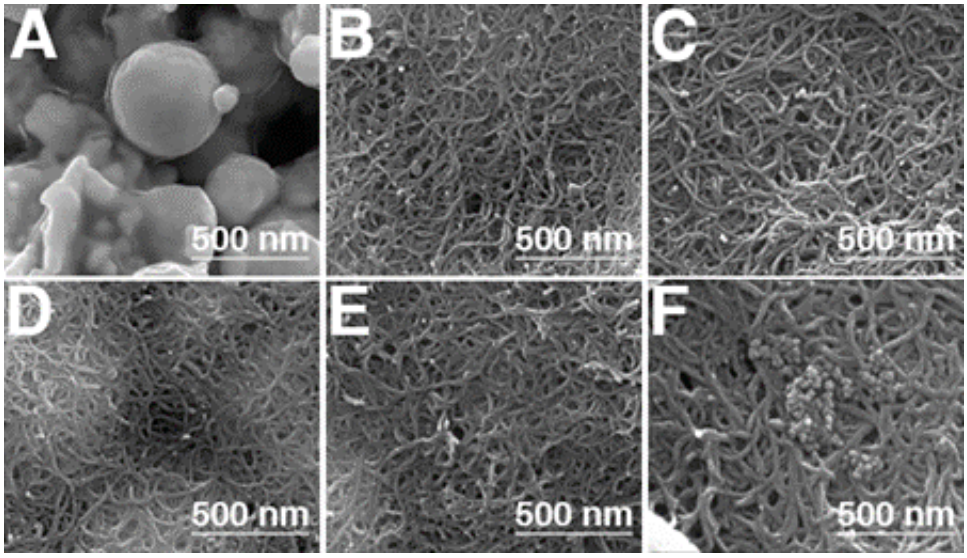

Figure 2.3. SEM images of **A.** bare AuSPE, **B.** AuSPE/MWNT-COOH, **C.** AuSPE/MWNT-COOH/Py-COOH, **D.** AuSPE/MWNT-COOH/Py-COOH/$Ab_{surface}$, **E.** AuSPE/MWNT-COOH/Py-COOH/ $Ab_{surface}$/BSA, and **F.** AuSPE/MWNT-COOH/Py-COOH/$Ab_{surface}$ /BSA/MNP-Ab_{HRP}-insulin (the presence of surface bound nanoparticle conjugates can be seen in the image).

Figure 2.4 shows the stepwise Fourier transform infrared spectroscopy characterization of the designed serum insulin immunosensor. MWNT-COOH coated electrodes displayed a C=O stretching at 1730 cm^{-1} and an O-H stretching at 3380 cm^{-1} (Figure 2.4-A). The characteristic C-H wagging vibration of Py-COOH was observed in Figure 2.4-B at 787 and 840 cm^{-1}.[57] With immobilization of proteins (i.e., $Ab_{surface}$ and BSA), amide-I C=O stretching and amide-II N-H bending peaks were observed at 1640 and 1550 cm^{-1}, respectively, along with an N-H stretching at ~3500 cm^{-1}.[18] Binding of serum insulin from the MNP-Ab_{HRP}-insulin conjugate onto the surface Ab of MWNT-COOH/Py-COOH/$Ab_{surface}$/BSA increased the intensities of amide-I and amide-II signals along with the C=O peak due to the formation of a sandwich immunoassembly featuring serum insulin molecules sandwiched between the $Ab_{surface}$ and Ab_{HRP}.

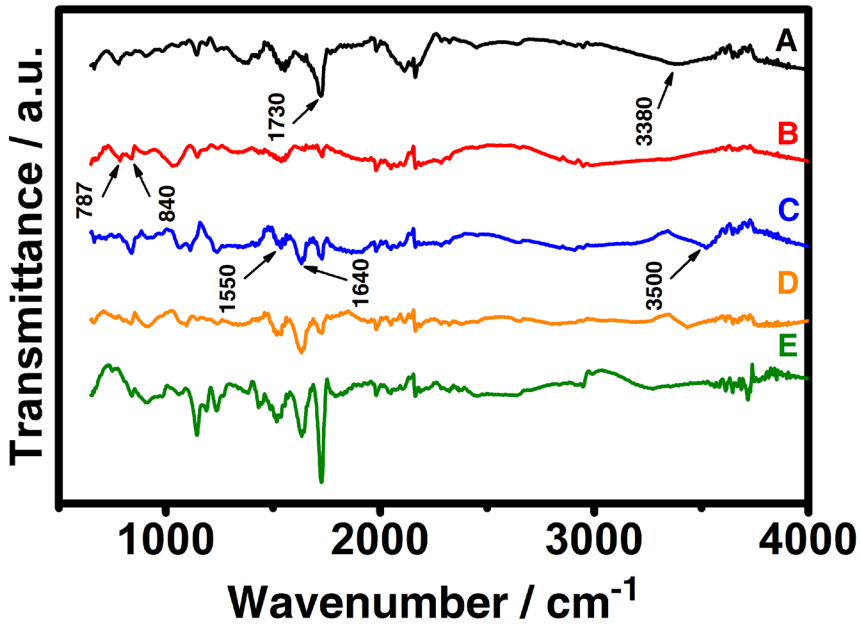

Figure 2.4. FTIR spectra of **A.** MWNT-COOH, **B.** after Py-COOH stacking, **C.** after covalent attachment of $Ab_{surface}$, **D.** after BSA blocking, and **E.** after binding of MNP-Ab_{HRP}-insulin conjugate prepared with 150 pM serum insulin concentration.

Figure 2.5 illustrates the stepwise Raman characterization of the immunosensor. Figure 2.5-A shows the characteristic D and G bands of MWNT-COOH that shifted to a lower frequency after π-π stacking with Py-COOH molecules.[58] The D and G bands shifted from 1354 and 1593 cm^{-1} to 1345 and 1588 cm^{-1}, respectively. This was attributed to the partial electron transfer from Py-COOH to MWNT-COOH and a relatively weaker C-C bond force constant on the hybrid complex than on nanotubes.[59] This confirmed that π-π stacking of Py-COOH molecules on the MWNT-COOH electrode occurred after the pyrenyl incubation over nanotubes. Figure 2.5-B shows the Raman spectra for every modification on the electrode surface. All spectra exhibited carbon related D, G, and 2D modes at approximately 1350, 1600, and 2900 cm^{-1}, respectively. After binding of the MNP-Ab_{HRP}-insulin conjugate (150 pM serum insulin treated) onto the surface insulin antibody, a weak phonon band for the Fe_3O_4 core of MNPs was observed at

approximately 150 cm^{-1}. Together, the spectral and microscopic studies confirmed the applicability of the designed immunosensor for serum insulin measurements.

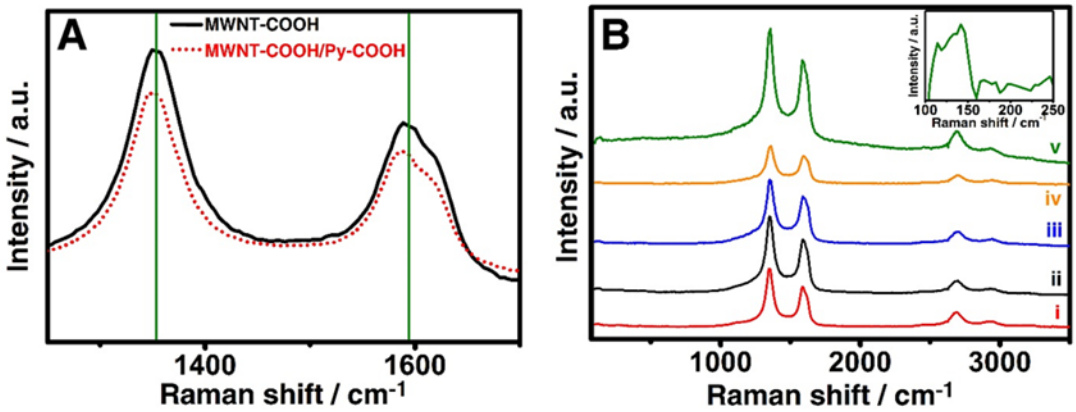

Figure 2.5. A. Raman spectra showing the D and G bands of MWNT-COOH shifted to lower frequencies after π-π stacking of Py-COOH molecules. **B.** Raman spectra of **i.** MWNT-COOH, **ii.** after Py-COOH stacking, **iii.** after covalent attachment of $Ab_{surface}$, **iv.** after BSA blocking, and **v.** after binding of MNP-Ab_{HRP}-insulin conjugate prepared with 150 pM serum insulin. Inset shows the weaker phonon band of magnetite core of MNPs in the MNP-Ab_{HRP}-insulin conjugate.

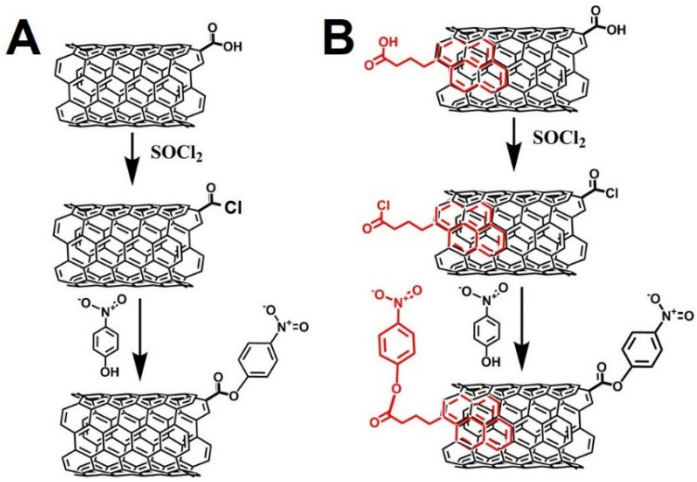

Figure 2.6. Conversion of carboxyl terminals into acyl chlorides and their derivatization with 4-nitrophenol for assessing electroactive surface coverage in **(A)** MWNT-COOH only, and **(B)** Py-COOH/MWNT-COOH.

Electrochemical quantitation of the surface –COOH groups in the two types of immunosensors (i.e., with and without Py-COOH) revealed 3.7 (± 0.7) x 10^{-10} mol/cm^2 of -COOH in MWNT-COOH/Py-COOH modified AuSPEs compared to 0.8 (± 0.1) x 10^{-10} mol/cm^2 of –COOH in the MWNT-COOH only modified AuSPEs. Quantitation of carboxyl groups was done by converting them to acyl chlorides followed by derivatization with 4-nitrophenol via an ester linkage.[60] This strategy was adopted for both immunosensors with and without π-π stacking of pyrenyl compounds (Figure 2.6). The voltammetric reduction of the arylnitro-labels on the surface allows for quantitation of carboxyl groups (Figure 2.7 for cyclic voltammograms).[60]

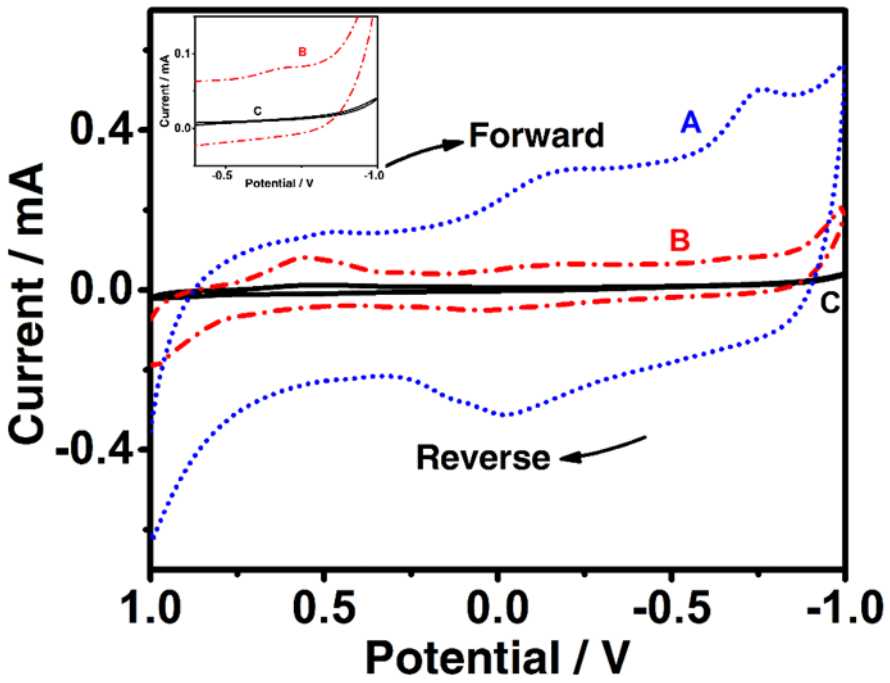

Figure 2.7. Cyclic voltammograms used for the quantitation of surface carboxyl groups based on the arylnitro derivative reduction peaks (at ~ -0.8 V) of **A.** MWNT-COOH/Py-COOH and **B.** MWNT-COOH modified on AuSPEs. This derivative peak is absent on **C.** bare AuSPE with no modification. Inset shows the enlarged view of the derivative peak of MWNT-COOH at ~ - 0.8 V **(B)**, which is absent on the bare AuSPE **(C)**. The measurements were done at 23 ˚C in phosphate buffer (pH 6.8, 25 mM KH_2PO_4, 25 mM Na_2HPO_4), scan rate 75 mV/s.

Thus, the higher number of –COOH groups available in the combined MWNT-COOH/Py-COOH modification (i.e., 4.6-times) could offer greater covalent attachment of $Ab_{surface}$ molecules than the MWNT-COOH modification alone on AuSPEs, which would result in enhanced serum insulin detection sensitivity (Figure 2.8). We quantitated $Ab_{surface}$ using the NanoOrange Protein Quantitation Kit (Thermo Fisher Scientific). The amount of $Ab_{surface}$ on the MWNT-COOH/Py-COOH modified AuSPEs was estimated to be 8.7 ± 2.5 pmol/cm^2, whereas it was 2.9 ± 0.4 pmol /cm^2 in the case of only MWNT-COOH modified AuSPEs. This quantitation confirmed that the combination of covalent and noncovalent carboxylations of MWNT allowed greater amount of immobilized $Ab_{surface}$ (about 3 times) compared to MWNT-COOH only modified AuSPEs.

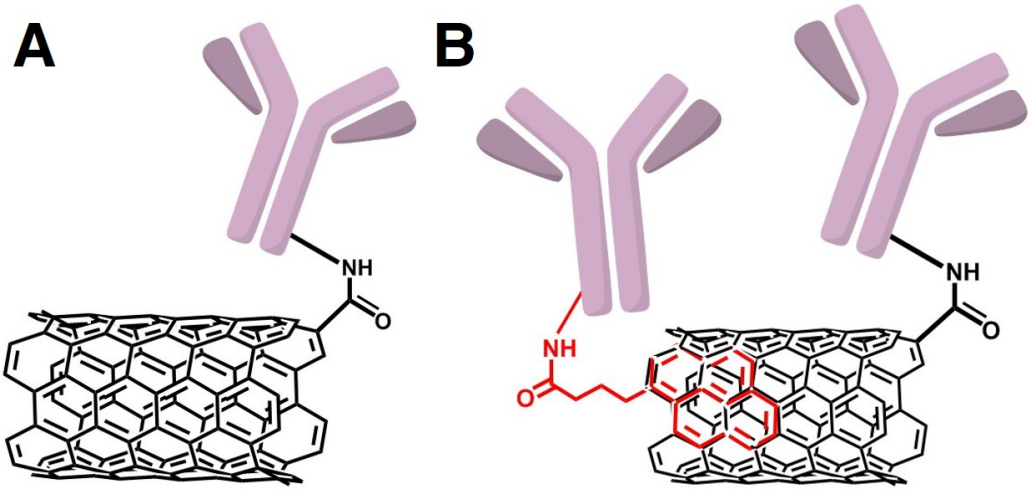

Figure 2.8 Strategy to enhance the number of antibodies immobilized in MWNT-COOH **(A)** by π-π stacking Py-COOH over MWNT-COOH **(B)**.

2.3.2 Amperometric responses relationship with insulin-magnetic nanoparticles conjugates

Figure 2.9-A shows the amperometric current signals for various serum insulin concentrations detected by the designed immunosensor. The amperometric trace for serum insulin of a 20-times diluted T2D patient's serum in PBS (that corresponds to 5% serum) is also shown in Figure 2.9-A. From the calibration plot of measured currents with insulin concentration, we determined the patient serum insulin concentration to be 340 ± 30 pM, which agreed with estimation by the standard enzyme-linked immunosorbent assay (commercial serum insulin kit, Mercodia Inc., Sweden) method.[17] As mentioned earlier, similar to the above immunosensor design of MWNT-COOH/Py-COOH/$Ab_{surface}$/BSA on AuSPEs, we designed a sensor without the Py-COOH linkers (i.e., MWNT-COOH/ $Ab_{surface}$/BSA on AuSPEs) for serum insulin measurements using the above described MNP-Ab_{HRP}-insulin conjugation strategy (Figure 2.9-B). Immunosensors without Py-COOH linkers offered lower current signals as well as a narrower dynamic range compared to sensors with Py-COOH linkers.

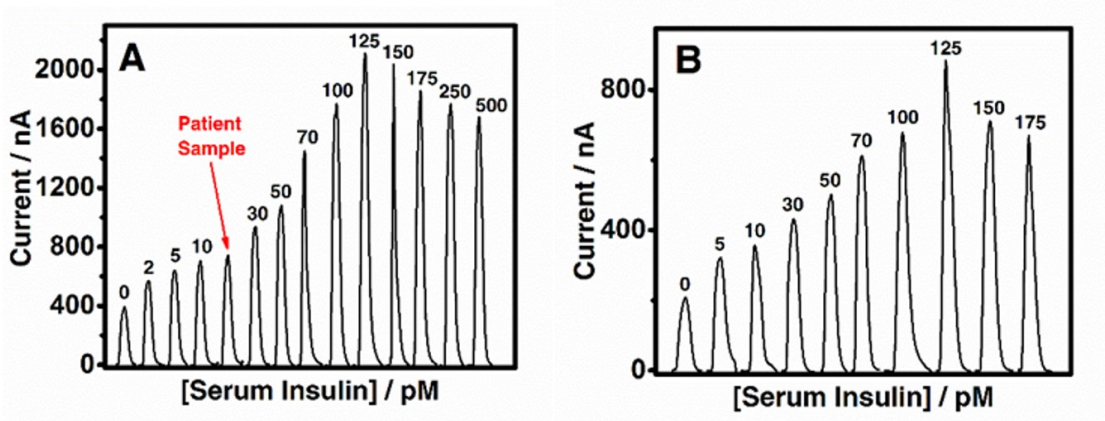

Figure 2.9. Immunosensor current signals with increasing serum insulin concentration in 5% serum captured onto MNP-Ab_{HRP} conjugates and upon binding to surface immobilized insulin-antibody on A. with and B. without Py-COOH linkers on MWNT-COOH coated AuSPEs. Experimental Conditions: - 0.1 V vs. pseudo Ag reference, 1 mM HQ, 0.5 mM H_2O_2, flow rate 200 µL/min, room temperature (23 ºC), N = 4 replicates.

Figure 2.10 (A and B) compares the current responses for different serum insulin concentrations measured by the two immunosensor strategies. The slope of the linear relationship plots between current and concentration corresponds to sensitivity. From the slopes, we determined that AuSPEs fabricated with the π-π stacked Py-COOH molecules on MWNT-COOH showed nearly 3-times greater sensitivity compared to those without the Py-COOH molecules (Figure 2.10).

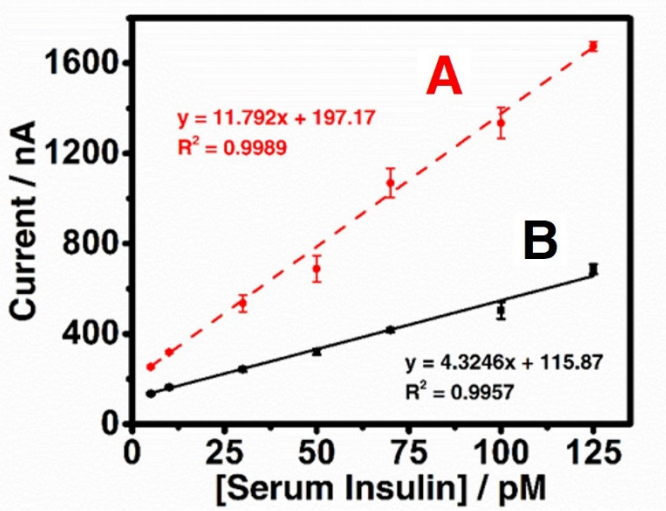

Figure 2.10. Current responses for immunosensor electrodes fabricated **A**. with and **B**. without Py-COOH linkers on MWNT-COOH coated AuSPEs for serum insulin detection (N = 4 replicates).

The linear range of the designed immunosensor with Py-COOH stacking was from 2-125 pM and for the sensor without the Py-COOH the linear range was from 5-125 pM serum insulin (Figure 2.10). This linear range is sufficient to differentiate type 1 (< 50 pM) from type 2 (> 70 pM) diabetes serum insulin levels under fasting conditions. The decrease in current signals at higher concentrations could have likely risen from the surface saturation of the electrode with MNP-Ab_{HRP}-insulin conjugates and resulting associated resistance for the communication of the electron transfer mediator with the electrode. More importantly, the sensitivity enhancement accomplished in this work by the combination of MWNT-COOH with Py-COOH is also

significant for diagnostic biosensors that measures elevated or diminished levels of disease biomarkers over normal conditions.

The limit of detection (LOD)[61] for serum insulin was calculated to be 1.5 pM for the Py-COOH stacked MWNT-COOH immunosensor electrodes and the LOD was 3.0 pM in the case of only MWNT-COOH modified immunosensor electrodes with no Py-COOH stacking. In addition, we observed better insulin affinity for $Ab_{surface}$ on the MWNT-COOH/Py-COOH modified AuSPE sensor (calculated apparent electrochemical Michaelis-Menten constant,[62] K_M^{app}, was 168 pM) than the MWNT-COOH only modified AuSPE sensor (K_M^{app} 270 pM) (Figure 2.11 for Lineweaver-Burk plots). This can be attributed to the greater number of available carboxyl groups provided by the combination of Py-COOH and MWNT-COOH for enhanced $Ab_{surface}$ attachment and in turn to more $Ab_{surface}$ binding sites for the binding of MNP-Ab_{HRP}-insulin conjugates with stronger affinity.

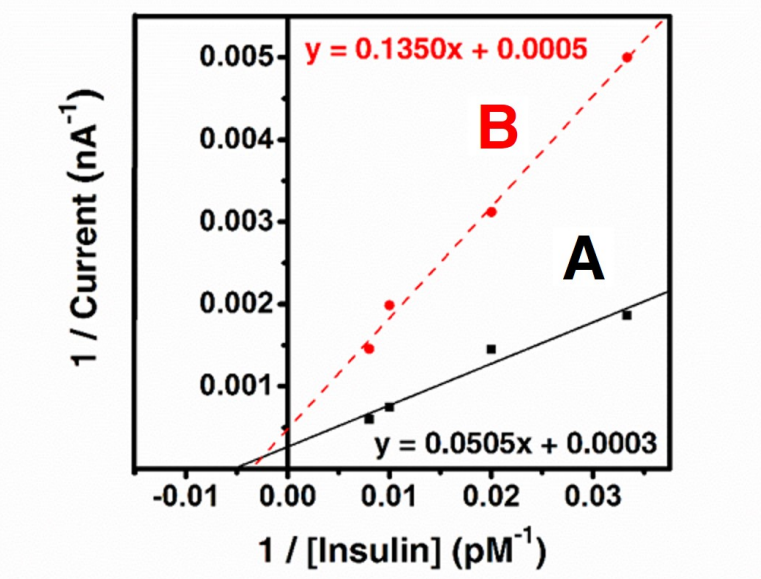

Figure 2.11. Lineweaver-Burk double reciprocal plots relating the changes in the measured redox mediator currents with the concentration of bound serum insulin onto $Ab_{surface}$ in the designed immunosensors: **A.** with and **B.** without Py-COOH linkers on MWNT-COOH coated AuSPEs.

2.4 Conclusion

In conclusion, we demonstrated the significance of combining covalent and noncovalent functionalization of carbon nanotubes for sensitive immunosensing applications. We applied the aforementioned surface chemistry to design and develop a novel amperometric immunosensor to measure serum insulin concentrations with diabetes relevant pM concentration levels. The results in this study suggest that the covalently functionalized carbon nanostructure-based sensors, drug delivery, and catalytic systems can benefit by additional incorporation of noncovalent pyrenyl or other similar noncovalent strategies to deliver improved performance. The presented surface design methodology is not limited to electrochemical detection because this combined covalent and noncovalent carbon nanostructure functionalization strategy can also be used for optical and spectral based detection methods and for any enzyme immobilized electrocatalytic applications. Similarly, the detection is not limited to serum insulin alone, any other biomolecules and small molecules can be also detected in principle utilizing the demonstrated combination of covalent and noncovalent functionalization of carbon nanotubes and other related carbon materials.

CHAPTER III

GRAPHENE MODIFIED SURFACE PLASMON MICROARRAY FOR SENSITIVE MEASUREMENT OF SERUM AUTOANTIBODY LEVELS WITH BINDING INSIGHTS

3.1 Introduction

Diabetes mellitus is a chronic disease that hampers the body's ability to use glucose and convert it to energy. This results in hyperglycemia, which can eventually lead to many fatal complications, including cardiovascular disease, neuropathy, and diabetic nephropathy. Due to changing lifestyles and environmental causes along with genetic factors, the number of people affected by diabetes is on the rise. According to WHO, diabetes was the seventh leading cause of death worldwide in 2016.

Traditionally, diabetes is divided into two categories based on how the body responds to insulin, which is a polypeptide hormone secreted in the islets of Langerhans in the pancreas. T1D results from genetic and environmental factors and is associated with the destruction of β-cells, which leads to insulin deficiency, and is also characterized by the appearance of autoantibodies against β-cell antigens namely: glutamic acid decarboxylase-65 (GAD-65), insulin, and tyrosine phosphatase-related islet antigen 2 (IA-2).[63,64] In contrast, T2D results from the body's inability to use the produced insulin.

Although diabetes is a serious medical condition, it can either be delayed or avoided with early prediction and maintenance of a healthy lifestyle. Consequently, it is essential to develop a tool that can fundamentally predict the susceptibility of a person to develop the disorder long before the clinical onset.

In recent years, the prevalence of diabetes, in particular T1D, is continuously increasing at a rate of 3% every year, and this in turn has impacted the incidence of associated lethal complications in children and adults likewise.[65] While the etiology of T1D is mostly unknown, a combination of genetic predisposition, environmental factors, and a dysfunctional immune system is believed to play a significant role in the development of the autoimmune disorder.[66-68] Numerous studies have reported that serum autoantibodies against the β-cell antigens are present in patient's biological fluids years before the clinical onset of diabetes.[69]

In the early 1990s, a 65 kDa autoantigen known as GAD-65 was identified to interact with an autoantibody, leading to the discovery of glutamic acid decarboxylase-65 autoantibody (GADA). GADA is the first line of clinical assessment in diagnosing the development of T1D, and its presence indicates the need for screening of other islet autoantibodies. A positive result for three or more autoantibodies suggests that the risk for developing T1D is 100% within the next 5 years.[70] Although the seropositivity for GADA varies with environmental, geographical, ethnic, and genetic factors, a general consensus reference value of ≤ 1.3 ng/mL is usually accepted as a normal condition.[27] Higher concentrations of GADA can indicate susceptibility to autoimmune diabetes and other endocrine disorders.

Over the past two decades, many research groups demonstrated several methods for clinical diagnosis of T1D including radioimmunoassay (RIA),[71] enzyme-linked immunosorbent assay (ELISA),[72] chemiluminescent immunoarray (CLIA)[73], and electrochemiluminescence assay[74]. These techniques are mostly time consuming (> 2 h), with RIA taking almost 2 days to

complete the analysis of a single autoantibody. Previous studies for GADA on surface plasmon resonance (SPR) platform mainly focused on surface modification techniques using self-assembled monolayer (SAM) of thiols and enzyme precipitation.[75-77] These studies mainly lacked in areas of clinical significance. Additionally, a few other studies demonstrated multiplexing of autoantibodies using plasmonic, electrochemiluminescence, and ELISA platforms, but most of them involved longer assay times and required chemical labels.[28-30] In contrast, magnetic beads (MAG)-based signal amplification labels are relatively more robust and allow easy conjugation of capturing biomolecules and isolation of target analytes, thus minimizing interference from the sample matrix in detection signals. In this context, surface plasmon resonance microarray imaging (SPRi)-based biosensing devices provide an effective tool for rapid, real-time, sensitive, and cost-effective detection of biological analytes in a complex system. SPRi is a label-free optical detection technique that provides a suitable and reliable platform for clinical analysis of biomolecular interactions and has many applications in biomedical science, bioengineering, proteomics, and genomics.[78] A SPRi-based diagnostic device is critical for better health management of the large diabetic population. It would be suitable for frequent monitoring of multiple analytes in a small sample amount (a few microliters of serum).[34]

As a novel class of two-dimensional nanocarbon materials, graphene and its derivatives have been extensively used in biomedical sciences for the development of electrochemical and optical biosensors.[79-81] The high surface area to volume ratio, electrical conductivity, aqueous dispersibility, thin structure, and apparent biocompatibility of graphene makes it a unique carbon nanomaterial for biorecognition events and biosensing applications.[82-84] Studies have shown that using graphene over a thin metal (gold or silver) surface enhances the SPR signals due to charge transfer from graphene to the metal, which leads to strong excited electric field enhancement at the surface.[85] In recent years, graphene has been used extensively alone or with metal composites to fabricate ultrasensitive biosensors for the detection of biomolecules, including cancer

biomarkers and DNA.[86,87] Graphene has great potential in the development of next generation biomolecular electronics and spintronic devices due to its electrical, optical, and thermal properties.[88,89]

In this study, an array-based biosensing device for the detection of GADA directly in clinical matrices was fabricated. Additionally, carboxylated graphenyl surface was quantitatively compared with the conventional 3-mercaptopropionic (MPA) monolayer surface to obtain analytical insights into the assay performance (Figure 3.1). Furthermore, binding parameters were also established for the GAD-65 antigen-autoantibody complexes as a quality control checkpoint. The knowledge gained from the combined sensing and binding assessment is useful for developing reliable, and better throughput clinical immunosensors for biomarker based diagnostic assays.

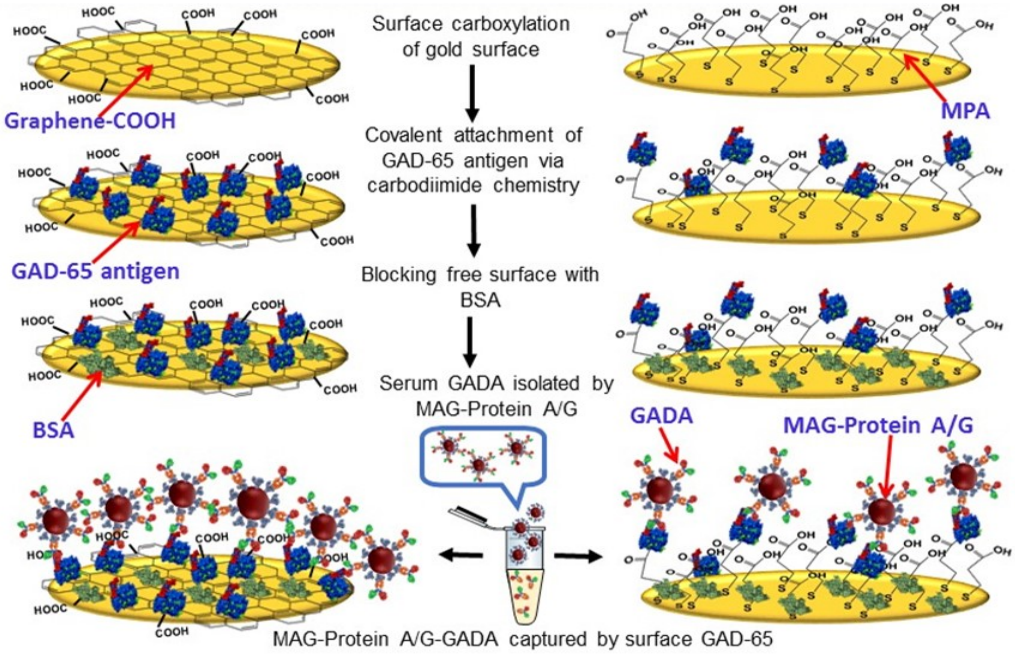

Figure 3.1. Graphenyl and mercapto- based immunosensor designs for comparative analysis of GADA detection.

This study was one-half of a project where we looked at electrochemical detection of serum GADA and correlated it with GADA detection in SPRi platform. The electrochemical part of the project was performed by previous group member Gayan Premaratne.

3.2 Experimental

3.2.1 Reagents and materials

8-channel screen-printed gold electrodes (8xSPE) were purchased from DropSens Inc., Spain (Product No. 8x220BT). SPR imaging (SPRi) gold array chips (Spot Ready 16, 1 mm diameter gold spots) were purchased from GWC Technologies (Madison, WI). Carboxylated graphene (graphene-COOH) was purchased from ACS materials (Medford, MA). Glutamic acid decarboxylase-65 antigen (GAD-65) was bought from Creative Diagnostics (Shirley, NY, USA). Monoclonal glutamic acid decarboxylase-65 autoantibody (GADA), bovine serum albumin (BSA, ≥ 98%), aminoferrocene, 3-mercaptopropionic acid (MPA, ≥99%), 1-ethyl-3-[3-(dimethylamino) propyl] carbodiimide (EDC), and *N*-hydroxysuccinimide (NHS) were purchased from Sigma (St. Louis, MO). Normal human serum was purchased from Atlanta biologicals (Flowery Branch, GA). Human serum samples were diluted 10-times in phosphate buffered saline (PBS), pH 7.4. Protein A/G coated magnetic beads (MAG-protein A/G, 2 μm, 10 mg mL^{-1}) were purchased from Biotool (Houston, TX). The beads contain 9.3×10^{13} protein A/G molecules/cm^2 (Biotool). All other chemicals used were analytical grade. The reagents were prepared using ultra-pure water (Invitrogen Corporation, Grand Island, NY). All measurements were conducted at room temperature (23 ˚C).

3.2.2 Instrumentation and methods

SPRi responses were obtained using a GWC SPR imager-II (Horizon SPR imager model). The SPR microarray imager was purchased from GWC Technologies (Madison, WI). The instrument's light source had an operating wavelength of 800 nm and had a charge coupled

device camera as the detector. The SPR curves were fit for kinetic analysis using TraceDrawer Software (Ridgeview Instruments AB, Vänge, Sweden).

Characterization of each step of the surface modification was conducted by scanning electron microscopy (SEM, Model: FEI Quanta 600FE) at an accelerating voltage of 20 kV. The images were acquired using FEIxT Microscope Control Software. Additional characterization of the sensor designs was conducted by Fourier transform infrared spectroscopy (FTIR, Thermo Scientific Nicolet iS50) operated in the attenuated total reflection mode using a diamond crystal.

XPS analysis of the surfaces of SPRi chip modified with graphene-COOH and MPA were performed using a Quantum 2000 Scanning ESCA Microprobe (Physical Electronics, Inc., MN) that features a monochromatic Al Kα x-ray source and an x-ray beam diameter of ≤ 100 μm (x-ray power ≤ 25 W), an automatic charge neutralization, depth and line profile analyzer, and an elemental mapping. The sample species were prepared by oven baking one gold SPRi chip drop-coated with the aqueous graphene-COOH at 50 ºC for 30 minutes while another gold SPRi chip was incubated overnight in MPA solution.

Raman spectroscopic analysis was performed with WITec alpha300 R confocal Raman microscope (WITec Instruments Corp., TN) using a laser power of 0.76 mW. The samples were prepared by oven baking the drop-coated aqueous graphene-COOH on a gold array spot of SPRi chip or on a glass surface as the non-gold control.

Cyclic voltammetric measurements were performed using a CHI 1040C electrochemical workstation (Austin, TX). Cyclic voltammetry was used for the quantitation of surface carboxyl groups of graphene-COOH and MPA by aminoferrocene derivatization of the –COOH groups.

3.2.3 Preparation of SPRi immunosensor

Figure 1 shows the schematic representation of the SPR immunosensor designed in this study. Prior to use, the SPRi gold array chip was cleaned in piranha solution (3:1 mixture of concentrated H_2SO_4 and 30% H_2O_2 for 10 seconds (Caution: Piranha solution is highly corrosive and a strong oxidizer)).

First, 0.30 µL of 0.1 mg/mL of carboxyl-functionalized graphene (graphene-COOH) was dry-coated on each gold spot of the SPRi chip and dried at 50 °C for 30 minutes. The chip was then washed thoroughly with water to remove any unbound molecules. Following dry-coating, the terminal carboxyl groups of carboxylated graphene were activated by converting them into *N*-succinimidyl esters after incubating it with 100 µL of a freshly prepared mixture of 0.4 M EDC and 0.1 M NHS in ultrapure DI water for 15 minutes. These esters facilitated covalent attachment of lysine residues from the GAD-65 autoantigen after incubating the chip with 100 µL of 100 nM GAD-65 prepared in PBS buffer for 30 minutes. After autoantigen immobilization, the surface was blocked with 100 µL of 1 % BSA in PBS for 30 min to minimize nonspecific binding. Then each spot was individually incubated with 0.25 µL a different concentration of 1 mg/mL MAG-protein A/G-autoantibody conjugate and the corresponding change in pixel intensity was observed. The chip was then mounted in the SPRi instrument to monitor real-time reflectivity changes upon the binding of various concentrations of serum GADA captured onto MAG-protein A/G beads. Once the steady state response was reached, the SPR chip surface was rinsed well with PBS (pH 7.4) to remove any unbound molecules present in the bulk solution and attain a new baseline signal. Similar SPR measurements were taken for an immunosensor prepared with a self-assembled monolayer of MPA instead of the graphene-COOH modification.

3.2.4 Preparation of magnetic bead-protein A/G-autoantibody conjugates (MAG-protein A/G-GADA)

MAG beads functionalized with surface protein A/G molecules offer binding sites with orientation for capturing antibodies from serum. The capturing procedure followed the instructions provided by the manufacturer with slight modifications. In brief, 25 µL of MAG-protein A/G bead was washed twice with 150 µL of phosphate buffered saline (PBS, pH 7.4, 10 mM phosphate, 0.14 M NaCl, 2.7 mM KCl), and separated out using a small piece of magnet after each wash. Then the beads were washed twice in 150 µL of binding buffer (50 mM tris, 150 mM NaCl, 0.1% Tween 20, pH 7.5). Different concentrations of GADA spiked in 10% normal human serum in the binding buffer (250 µL) were added to separate aliquots of MAG-protein A/G beads and rotated in a tube rotor (Fisher scientific) for 1 h at room temperature. Upon completion of the incubation, the contents were suspended by pipetting in and out for 10 times, and the supernatant was removed immediately from the magnetically separated beads. The beads were washed two times with 300 µL of the binding buffer. Finally, the beads were suspended to a final volume of 200 µL in the binding buffer. The MAG-protein A/G captured serum GADA samples were stored at 4 ^{o}C and used for up to 5 days.

3.2.5 Quantitation of surface carboxyl groups based on electroactive aminoferrocene labels

8xSPEs were dry-coated with graphene-COOH or with a self-assembled monolayer of MPA (one 8xSPE was used for each modification) followed by carbodiimide activation of the surface carboxyl groups using the 0.4 M EDC and 0.1 M NHS solution mixture. Then a 4.5-µL solution of 1 mM aminoferrocene in PBS, pH 7.4 was placed on the –COOH activated electrodes and incubated for 45 min in a cold and moist atmosphere. To ensure the covalent strategy of linking, we prepared graphene-COOH or MPA modified 8xSPEs with an electrostatically adsorbed layer of aminoferrocene. Then the electrodes were rinsed with deionized water to remove any unbound

molecules. Cyclic voltammograms (CVs) were recorded to calculate the electroactive aminoferrocene molecules, and in turn the relative amounts of –COOH groups on graphene-COOH and MPA surfaces.

3.3 Results and discussion

3.3.1 Assessment of plasmonic enhancement property of the graphene-gold complex

To illustrate the plasmonic enhancement property of graphene-COOH on the Au surface of the designed sensor,[90] we performed Raman spectral analysis of the graphene-COOH coated on the gold surface of a SPRi chip and compared the spectral peak intensity with similarly coated graphene-COOH on a plain glass instead of gold (Figure 3.2). The Raman signal for the D band at ~1350 cm^{-1} and G band at ~1600 cm^{-1} shows about 5.5-times signal enhancement for graphene-COOH coated on the Au surface compared to the glass substrate. The increase in Raman signals has been proposed to be due to a charge-transfer process from the graphenyl material to the gold metal surface resulting in the coupling of metal plasmons with graphene plasmons and the associated enhancement of electromagnetic fields.[86, 91]

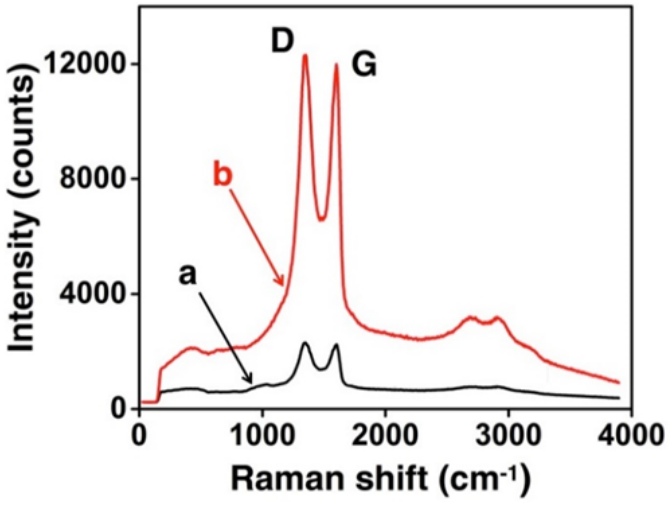

Figure 3.2. Raman spectra for graphene-COOH dry coated on **(a)** glass or **(b)** gold surface of an SPR chip.

3.3.2 Immunosensors characterization

The SEM images acquired at each step of the immunoassembly are presented in Figure 3.3 – A to D. Figure 3.3-A shows the image for a rough Au surface. Dry coating of graphene-COOH on the Au surface resulted in spherical mesh-like and thread-like features (Fig. 3.3-B).[92] The graphene surface feature became denser upon the covalent immobilization of GAD-65 antigen followed by blocking with a solution of 1% BSA in PBS (Fig. 3.3-C). After the binding of the MAG-protein A/G-GADA conjugate onto the surface GAD-65 sites, the appearance of spherical MAG bead features on the electrode surface can be seen (Fig. 3.3-D).

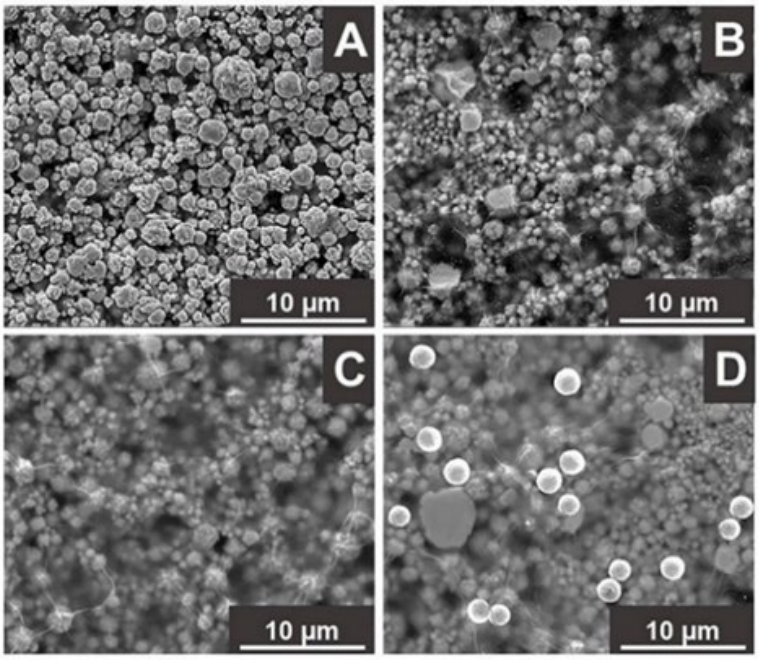

Figure 3.3. SEM images of **A.** rough Au surface, **B.** after dry coating of an aqueous suspension of graphene-COOH, **C.** after covalent attachment of GAD-65 antigen and surface blocking with 1% BSA, and **D.** after the binding of GADA spiked in 10% human serum and captured onto MAG-protein A/G beads.

FTIR spectra further confirmed the results obtained from the SEM image analysis. The bare Au surface did not show any significant peak in the measured vibrational region of the IR spectrum (Figure 3.4-A). Upon coating with graphene-COOH (Figure 3.4-B), the appearance of a strong and broad peak at about 3219 cm^{-1} was attributed to the hydroxyl vibration of the surface carboxyl groups.[93] Additionally, the peaks at 1719 cm^{-1} and 1078 cm^{-1} are characteristics of the stretching vibrations of carboxylic acid and other surface carbonyl groups.[94] Upon activation of the surface carboxyl groups using EDC/NHS chemistry, the characteristic decrease in the O-H stretching vibration was observed (Figure 3.4-C). Additionally, new peaks centered at 1764 and 1043 cm^{-1} corresponding to the C=O and C-O stretching vibrations of the succinimidyl esters from the EDC/NHS modification were present.[95,96]

The protein amide-I at 1639 cm^{-1} and amide-II at 1547 cm^{-1} were observed due to the formation of amide bonds after the covalent attachment of the GAD-65 antigen with the graphene-COOH surface (Figure 3.4-D).[97] In addition, a new peak at 3324 cm^{-1} indicated the N-H stretching vibration of the protein. When the serum GADA carried by the MAG-protein A/G beads bound to the surface GAD-65 antigen, a new peak appeared at 602 cm^{-1} that was assigned to the Fe-O stretching of Fe_3O_4 magnetic beads (Figure 3.4-E).[98] Furthermore, a slight shift in the amide-I and amide-II bands was possibly the result of complexation of GAD-65 with GADA. Additionally, the N-H bending vibration peak at 794 cm^{-1} became more prominent due to the overall increase in the total protein molecules on the surface as the result of GADA-GAD 65 immunoassembly formation.

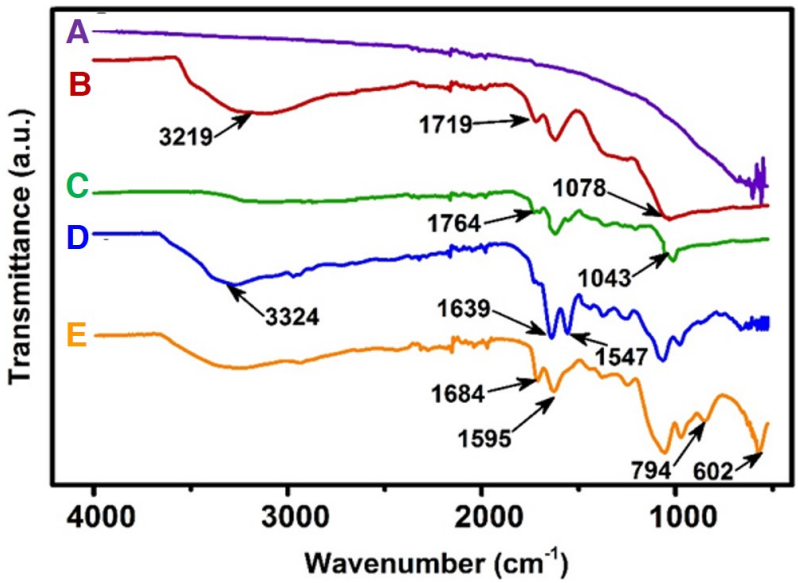

Figure 3.4. FTIR spectra of **A.** rough gold 8xSPE, **B.** after dry-coating with graphene-COOH, **C.** after EDC/NHS activation, **D.** after GAD-65 immobilization, and **E.** after the binding of 5 ng-mL^{-1} concentration of 10% serum GADA captured by the MAG-protein A/G beads.

The C1s region in the XPS spectra of graphene-COOH coated or MPA monolayer on the gold surface are presented in Figure 3.5. The XPS data were analyzed for carbon atoms from different functional groups such as C-C at 284.8 eV, C-O in epoxy/ether at ~286.0 eV, and C=O at ~288.0 eV.[99,100] As expected, the carboxyl groups on the graphene-COOH surface are greater than the MPA modified gold surface, which would thus provide greater sites for covalent attachment of GAD-65 antigen via amide bonds. The XPS finding correlated well with the electroactive quantitation of surface–COOH linked aminoferrocene molecules as discussed below.

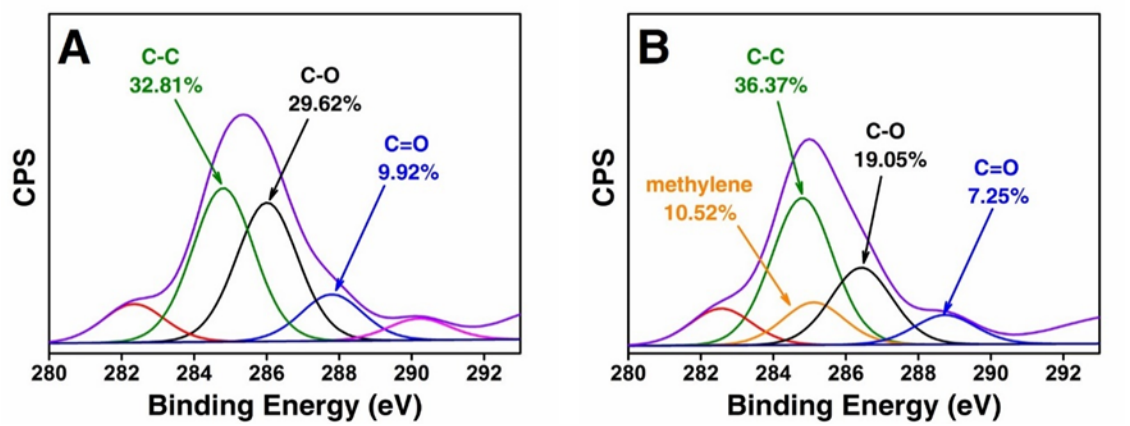

Figure 3.5. XPS spectra in the C1s region of **A.** Graphene-COOH coated gold SPR chip, and **B.** self-assembled monolayer of MPA on a gold SPR chip.

3.3.3 Estimation of the relative surface carboxyl groups on graphene-COOH and MPA modified gold surfaces

Figure 3.6-A and B represents the cyclic voltammograms of the graphene-COOH and MPA electrodes with covalently attached and electrostatically adsorbed redox active aminoferrocene molecules (voltammograms-a and b in each plot respectively). Integrated peak areas are directly proportional to the amount of electroactive aminoferrocene molecules bound to either graphene-COOH or MPA surface. The average formal potentials of the covalently attached aminoferrocene film on the graphene-COOH and MPA surfaces were 112 ± 5 and 114 ± 8 mV, respectively. The electrostatically adsorbed films of aminoferrocene on each of the modified surfaces exhibited a similar formal potential as the covalent films. However, the covalent films enabled higher electroactive aminoferrocene immobilization than the electrostatic films.

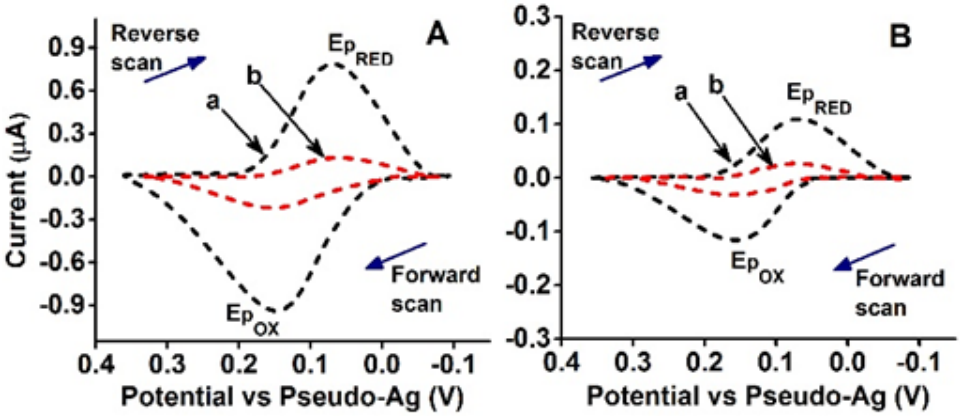

Figure 3.6. Background subtracted CVs of **A.** graphene-COOH, **B.** MPA modified gold electrodes with **a.** covalently attached, and **b.** adsorbed films of aminoferrocene in argon purged PBS buffer, pH 7.4, 23 °C. The scan rate was 0.1 V s^{-1}.

From the oxidation peak area, the electroactive surface coverage (Γ, Equation 3.1) of aminoferrocene and in turn, the relative amount of carboxyl groups were determined.[101] Q is the area of the oxidation peak of aminoferrocene, n is the number of electrons involved in the aminoferrocene oxidation (n = 1), F is the Faraday's constant, and A is the area of the working electrode (A = 0.2 cm^2).

$$\Gamma = Q / (nFA) \qquad \text{(Equation 3.1)}$$

Graphene-COOH surface provided a 9-fold greater surface carboxyl groups than the MPA monolayer surface for the covalent films (Table 3.1).

Table 3.1. Relative estimation of electroactive amounts of aminoferrocene on graphene-COOH and MPA modified electrodes.

Parameter		Graphene-COOH	MPA
Covalently attached aminoferrocene labels	Q (nC)	920.3 ± 86.6	98.1 ± 5.9
	Calculated Γ (pmoles/cm^2)	47.6 ± 5.1	5.1 ± 0.3
Adsorbed aminoferrocene labels	Q (nC)	189.4 ± 15.4	31.0 ± 1.9
	Calculated Γ (pmoles/cm^2)	9.8 ± 1.3	1.6 ± 0.11

3.3.4 Electrochemical detection of serum GADA concentrations

The identical immunosensing strategy was used to detect serum GADA concentrations in an 8-channel screen-printed gold electrodes (8xSPE) electrochemical array using faradaic electrochemical impedance spectroscopy (EIS). Faradaic impedance measurements for various concentrations of MAG-protein A/G captured serum GADA (10% normal human serum) bound onto GAD-65 were performed at room temperature (23 ^{o}C) in an aqueous electrolyte solution containing 0.1 M KCl and 10 mM each of $Fe(CN)_6^{3-}/Fe(CN)_6^{4-}$ as the redox probe. A potential of 0.2 V vs. a pseudo Ag reference electrode was applied at an AC amplitude of 10 mV, and the frequency was scanned from 100,000 – 100 Hz. The experimentally obtained Nyquist plot data were fit by the Randles equivalent circuit model to determine the charge transfer resistance (R_{ct}) values.

The Faradaic impedance responses and the respective calibration plots are presented in Figure 3.7-A to D. The R_{ct} of GAD-65 sensor surface increased with the binding of increasing

serum GADA concentration (10% serum in PBS) captured with the MAG-protein A/G beads. The detection sensitivity enhancement by the graphene-COOH modification compared to a conventional self-assembled monolayer surface on gold was also studied using MPA modified surface.

The results obtained indicated that the graphenyl sensor displayed a wider dynamic range of 0.02–2 ng mL^{-1} and several thousands of increased R_{ct} values over the MPA monolayer modified sensor (0.04–0.75 ng mL^{-1}) for the same GADA concentration. A sensitivity enhancement of about 3-fold was observed for the graphenyl surface over the MPA modified surface.

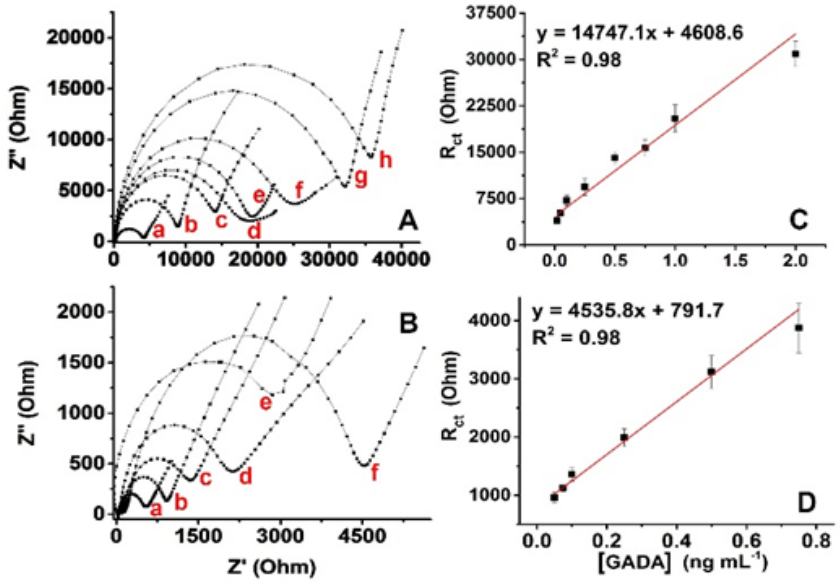

Figure 3.7. Nyquist plots for the Faradaic impedance measurements in an aqueous solution containing 0.1 M KCl and 10 mM each of $Fe(CN)_6^{3-}/Fe(CN)_6^{4-}$ for various concentrations of surface bound serum GADA immunoassembly on: **A.** graphenyl (a. 0.02, b. 0.05, c. 0.1, d. 0.25, e. 0.5, f. 0.75, g. 1.0, and h. 2.0 ng mL^{-1}) and **B.** MPA (a. 0.02, b. 0.05, c. 0.1, d. 0.25, e. 0.5, and f. 0.8 ng mL^{-1}) modified immunosensors. **C** and **D** represent the calibration plot of respective response plots for R_{ct} changes with concentration of GADA. (N = 3 replicates.)

3.3.5 SPRi pixel intensities for various serum GADA concentrations

The low dielectric permittivity and intrinsic graphene plasmonics with the ability to modulate the evanescent wave[92,102] allowed us to construct the immunosensor assembly on an SPR gold array chip to detect serum GADA and additionally obtain binding kinetic parameters. Increase in SPRi pixel intensities with increased concentration of serum GADA for graphene-COOH and MPA modified immunosensors are illustrated in Figures 3.8 -A and B, respectively. The nonspecific binding signal for MAG-protein A/G treated serum with no spiked GADA was taken as the control response. The control signal was lower for the graphene-COOH sensor compared to the mercapto modified sensor demonstrating that BSA blocked graphene-COOH surface is better than the conventional gold-MPA surface to minimize nonspecific signals. The results confirm that the assay specificity is based on the selective GADA and GAD-65 interaction.

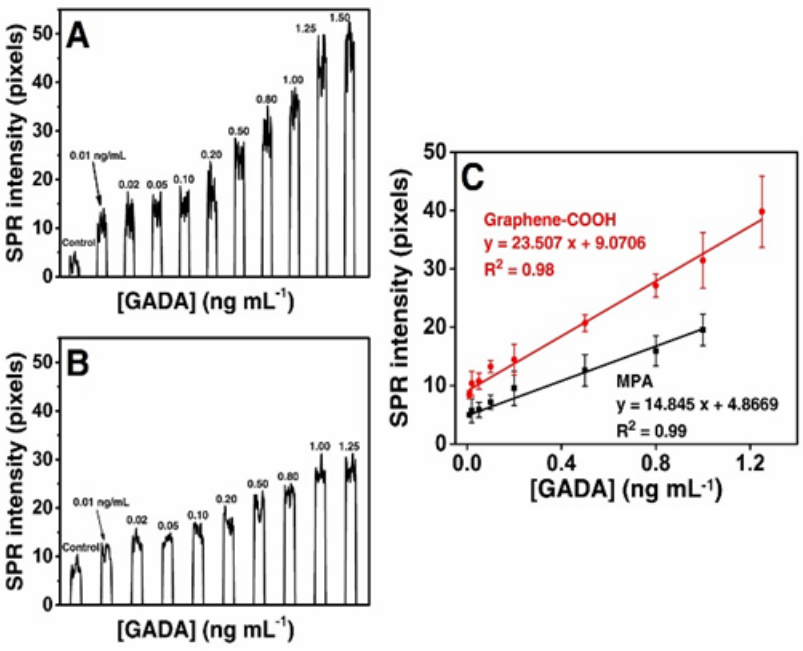

Figure 3.8. SPRi pixel intensities for different concentrations of serum GADA captured by MAG-protein A/G beads and bound onto GAD-65 antigen immobilized on **A.** graphene-COOH and **B.** MPA modified gold array chip. Control responses in A and B correspond to signals for the binding of 10% serum treated with MAG-protein A/G beads without spiked GADA. **C.** Control subtracted SPRi response plots with concentration of serum GADA for the GAD-65 immobilized graphene-COOH or MPA surface. (N = 4 replicates.)

Figure 3.8-C illustrates the linear range of SPRi response plots for varying concentrations of 10% serum GADA captured onto MAG-protein A/G beads and bound to the surface immobilized GAD-65 on both graphene-COOH and MPA surface. Graphene-COOH modified sensor was almost 2-times more sensitive than the MPA modified sensor. For the graphene-COOH sensor, the SPRi dynamic range was 0.01–1.25 ng mL^{-1} with 3-times lower detection limit (6.5 pg mL^{-1}) than the MPA sensor with a dynamic range of 0.01–1.00 ng mL^{-1} and a detection limit of 18.8 pg mL^{-1}.

3.3.6 Determination of kinetic parameters from the real-time binding of surface immobilized GAD-65 with MAG-protein A/G beads captured serum GADA

The kinetic analysis[103] was performed for the biomolecule interaction by assuming a 1:1 binding reaction as detailed below:

$$A+B \rightleftharpoons AB \qquad (3.2)$$

Rate of association: $$\frac{d[AB]}{dt} = k_a[A][B] - k_d[AB] \qquad (3.3)$$

Rate of dissociation: $$\frac{d[AB]}{dt} = - k_d[AB] \qquad (3.4)$$

Where, A is the GAD-65 antigen immobilized on the SPR chip, B is the GADA captured MAG-protein A/G beads, and AB is the antigen-antibody complex formed. Since the concentration of A is constant, the antigen-antibody complex formation is considered to follow a pseudo first order kinetics, where the SPR responses of the interaction with time is given as:

$$\frac{dR}{dt} = k_a C R_{max} - (k_a C + k_d) R_t \qquad (3.5)$$

The integrated form of (3.5) is given as:

$$R_t = \frac{k_a C R_{max}\left[1-e^{-(k_a C + k_d)t}\right]}{k_a C + k_d} + R_0 \qquad (3.6)$$

$$K_D^{app} = \frac{k_d}{k_a} \qquad (3.7)$$

Where, R_t and R_o are the SPR responses at any time t and at t=0 respectively, R_{max} is the maximum reflectivity change, C is the concentration of serum GADA captured onto MAG-protein A/G beads, k_a is the apparent association rate, k_d is the apparent dissociation rate, and K_D^{app} is the apparent binding constant. The values of k_a and k_d were obtained by fitting the experimental SPR curves using the TraceDrawer kinetics software (Figure 3.9).

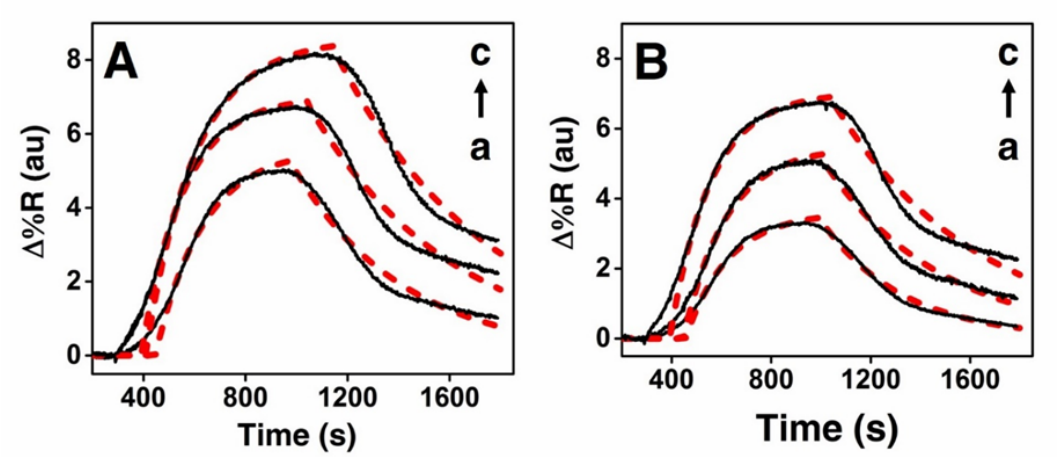

Figure 3.9. Simulated (red) and real-time SPR sensograms (black) representing different concentrations (a to c) of 10% serum GADA, 0.05, 0.10, and 0.50 ng/mL, captured with MAG-protein A/G beads and bound onto GAD-65 immobilized sensor surfaces modified with **A.** graphene-COOH and **B.** MPA.

The kinetic parameters comprising association rate (k_a), the dissociation rate (k_d), and the binding constant (K_D) for both graphenyl and mercapto surfaces are presented in Table 3.2.

Table 3.2. Kinetic parameters for the MAG-protein A/G beads captured serum GADA binding onto a SPRi surface immobilized with GAD-65 antigen.

Kinetic parameters	Graphene-COOH	MPA
Association rate constant, k_a [M^{-1} s^{-1}]	1.05 (± 0.13) × 10^9	0.90 (± 0.13) × 10^9
Dissociation rate constant, k_d [s^{-1}]	3.2 (± 0.4) × 10^{-3}	5.0 (± 0.6) × 10^{-3}
Binding constant, K_D [pM]	3.0 ± 0.5	5.6 ± 1.0

The lower K_D value for the graphene-COOH modified SPRi chip suggests that graphene provides a stronger GADA-GAD-65 binding interaction platform through its increased number of surface carboxyl groups and plasmon enhancing feature when compared to the mercapto monolayer modified chip. Moreover, the K_D values of both MPA and graphene-COOH modified chips are smaller (i.e., better affinity) in comparison to the previously reported SPR assay value (K_D = 1.37 nM) in PBS buffer medium on the surface of a mixed self-assembled monolayer.[104] This is possible due to the signal enhancements from the MAG-protein A/G bead strategy offering a highly enhanced signal output than free GADA present in solution. Moreover, MAG-bead based strategy was shown to allow a significantly greater amount of immobilization of surface antibodies due to the large number of particles with the net high surface area.[105] The high-density antibody carrying MAG-beads are expected to facilitate a greater rate of association with surface immobilized GAD-65 molecules and a slower dissociation when the interactions are strong (Table 3.2). A previous report estimated that over 100,000 molecules of antibody can be bound selectively to MAG-beads (1 μm) that facilitated attomolar detection limits of prostate specific antigen.[55]

3.4 Conclusion

Here, we presented an SPR immunoarray that can detect low levels of GAD-65 autoantibody in a serum matrix. The SPR microarray imager provided detection of the autoantibody-autoantigen interaction without the need of any chemical or enzymatic detection labels. The detection was based on the use of MAG-protein A/G bead-based signal amplification, which also allowed easy isolation and separation of serum autoantibody for detection in the antigen array. Additionally, MAG beads offered better sensitivity and selectivity of the autoantibody analyte signal compared to control serum samples. In comparison, plasmon enhancing graphene-COOH sensor offered higher sensitivity and selectivity with wider detection window than MPA sensor for GAD-65 autoantibody detection. The application of large surface area graphene for high density covalent attachment of GAD-65 enabled us to achieve a low detection limit of 6.50 pg/mL of GAD autoantibody. Additionally, graphene-based sensor offered higher specificity by reducing the background signals. This SPR microarray methodology is an attractive and promising tool for reliable diagnostics and early prediction of T1D based on autoantibody levels. The binding constant parameter can be used as a quality control checkpoint for large-scale production of graphenyl biosensors to implement for reliable applications in clinical diagnostic assays. Furthermore, the microarray surface design and detection strategy presented would be suitable for measuring any other serum biomarkers of significance present in clinical matrices.

CHAPTER IV

PAPER-BASED LABEL-FREE NON-FARADAIC IMPEDANCE AGAINST ENZYME CORRELATED AMPEROMETRIC SENSOR FOR SMALL MOLECULE DIABETIC INSULIN DETECTION

4.1 Introduction

A "biological marker" or a biomarker is a molecule that can be an indicator of normal versus abnormal condition and can help in disease diagnosis and health monitoring.[106] It has a broad applicability in areas of early diagnosis, disease prognosis, and monitoring clinical response to a therapeutic intervention. The field of biomarker study is so widespread that there are numerous studies dedicated to identification of biomarkers in different clinical matrices for various diseases ranging from Parkinson's, Alzheimer's, cancer, diabetes, and many others.[107-110] While, there are several studies dedicated to design of sensors for detection of such biomarkers in different biological matrices, very few of these sensors are successfully translated into medical devices. The shortcomings of such sensors are in the areas of selectivity, specificity, limit of detection, dynamic range, reproducibility, and non-specific bindings due to complex biological matrices.[111-113] This gets even more complicated whenever low molecular weight markers with ultralow concentrations in biological matrix are to be detected.

We chose one such molecule in this study as a model system, which is measuring picomolar concentrations of insulin in human serum relevant to pancreatic disorders. Insulin is a

small globular protein with two chains: the A chain has 21 residues and the B chain has 30 residues which are connected to each other by two disulfide bridges and has a molecular weight of 5808 Da.[114] In this paper, we will use insulin as our "small biomolecule model" to demonstrate paper-based electrochemical platform for both label-free and labeled detection of serum insulin molecules with clinically significant dynamic range and limit of detection.

Prior studies, including the ones from our research group, have extensively investigated the detection of insulin molecules in both electrochemical and optical platforms.[20,115,116] However, in the past few years the paradigm has shifted towards label-free detection including direct oxidation of insulin molecules.[21,117,118] This label-free strategy of biomolecules detection aligns with the guidelines for selecting a diagnostic tests set by the World Health Organization.[119] In this study, *in lieu* of expensive labeled detection techniques, we are presenting a paper-based label-free detection strategy of serum insulin molecules using non-faradaic impedance spectroscopy as denoted in Figure 4.1. Carboxylated graphene is dry coated on the working electrode which is used to immobilize aptamers produced against insulin, which in turn can selectively bind to insulin molecules in the serum samples. Capacitance is measured before and after the binding of insulin molecules and is represented as the relative changes as the detection signals. The capacitance (C) of a double layer interface is given by Equation 4.1.

$$C = \frac{\varepsilon_0 \varepsilon_r A}{d} \qquad \text{(Equation 4.1)}$$

Here, ε_0 and ε_r are the permittivity of free space and the dielectric constant of the material between the electrode and the mobile charges respectively, A is the surface area of the electrode, and d is the distance between the electrode and the mobile charges.[120] Hence, the capacitance changes when the distance or dielectric properties in the material between the electrode and mobile charges changes.

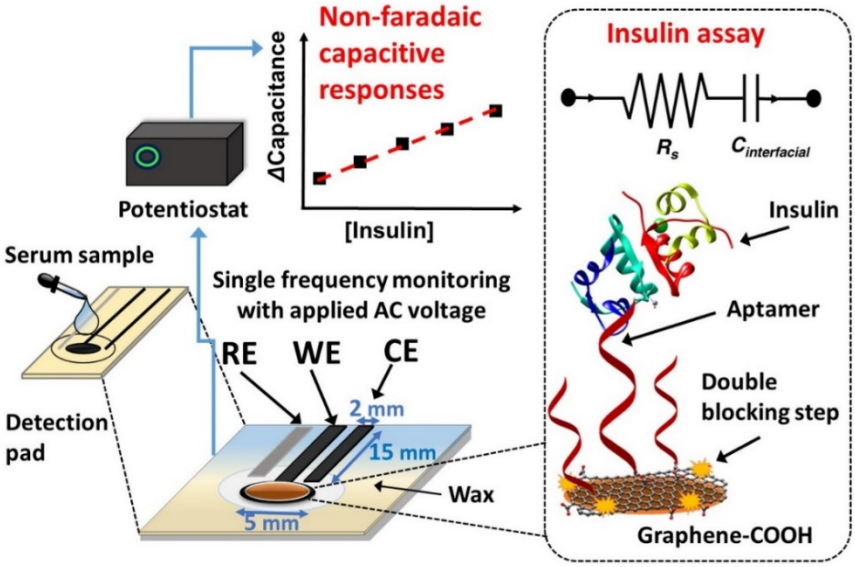

Figure 4.1. Paper electrode design with dimensions along with sensor surface modification strategy for capacitive detection of serum insulin.

Graphene is a novel class of two-dimensional carbon nanomaterial of significant interest in the scientific community due to its high surface area, high conductivity, high elasticity, and rapid electron transfer rates.[121,122] Graphene has found prominence in both electrochemical and optical sensing for biomolecule detection and signal amplification techniques, and in energy storage.[123-126] In relation to this study, we selected carboxylated graphene more specifically due to increased biomolecule immobilization sites, aqueous dispersibility, and biocompatibility.[127]

Aptamers are single stranded oligonucleotides synthesized by SELEX (Systematic Evolution of Ligands by Exponential Enrichment) that can fold into 3-dimensional shapes capable of binding non-covalently with an analyte with high specificity, stronger affinity, and longer stability, and are convenient in synthesis when compared to antibodies.[128,129] Upon recognition of binding analyte, they undergo a conformational change thus creating a specific binding site for that particular analyte. This folding can result in different kinds of structures such as stems, loops, bulges, knots, triplicates, hairpin, and G-quadruplex structures.[130] Analogous to

an antibody-antigen interaction, the nucleobases of the aptamers exhibit intermolecular interactions with the aromatic compounds of the target molecules along with additional electrostatic interactions and hydrogen bonding.[131-133]

Furthermore, we also have validated the applicability of the designed immunosensor assembly using enzymatic labels and monitoring amperometric signals as shown in Figure 4.2. This experimental technique is similar to one of our prior studies using screen printed electrodes as demonstrated in Chapter II.[134] The paper assembly is similar to the one used in capacitive sensing however, after insulin incubation, HRP labeled second insulin antibody is incubated on the sensor surface for another 30 min. After washing the electrode, thus prepared sensor is connected to a potentiostat and monitored for current signals while applying -0.1 V and adding 200 µL of a mixture of 1 mM hydroquinone and 0.5 mM H_2O_2. This study is different from our above mentioned prior study in that it uses paper substrate as the electrode setting and does not uses pump to flow the mixture of hydroquinone and H_2O_2 over the sensor surface.

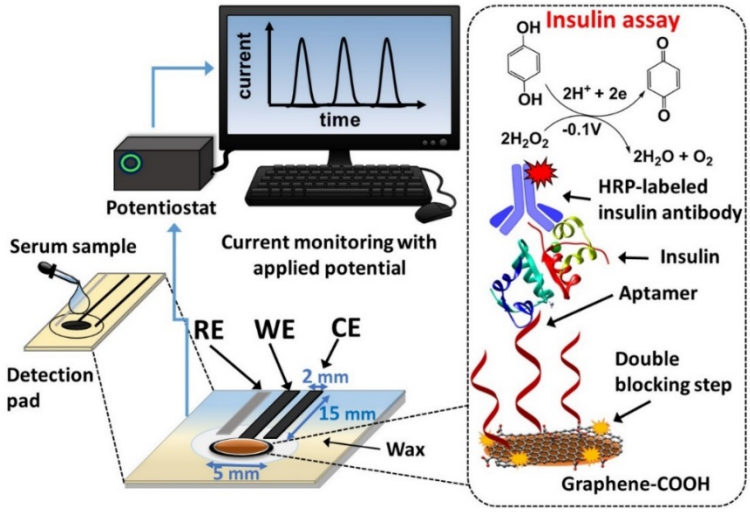

Figure 4.2. Paper electrode design similar to capacitive sensor with the exception of detection strategy using HRP labeled second insulin antibody and monitoring amperometric currents.

4.2 Experimental

4.2.1 Reagents and materials

GE Healthcare Whatman Grade 1 Chr Cellulose Chromatography Paper was purchased from Fisher Scientific (Hampton, NH). Graphite and Ag/AgCl ink were purchased from Ercon Inc. (Wareham, MA). Candle wax was purchased from a local Walmart supermarket. Carboxylated graphene was obtained from ACS Material, LLC (Pasadena, CA). N-(3-Dimethylaminopropyl)-N′-ethylcarbodiimide hydrochloride (EDC), N-hydroxysulfosuccinimide (NHS), bovine serum albumin (BSA), ethanolamine (EtOH-NH_2), aminoferrocene, hydrogen peroxide solution (H_2O_2), and hydroquinone (HQ) were purchased from Sigma-Aldrich (St. Louis, MO). Aptamers for insulin were purchased from Integrated DNA Technologies (Coralville, IA). The insulin aptamers were C6 amino modified (AmMC6) at the 5' terminal and the sequence was: 5' AmMC6/GGT GGT GGG GGG GGT TGG TAG GGT GTC TTC 3'. Recombinant human insulin (> 99%) was purchased from Kerafast, Inc. (Boston, MA). Horseradish peroxidase (HRP)-labeled rabbit polyclonal anti-insulin antibody (Ab_{HRP}) was purchased from LifeSpan BioSciences, Inc. (Seattle, WA). Insulin depleted human serum was purchased from Fitzgerald Industries International Inc. (Acton, MA). A diabetic patient serum sample was purchased from BioIVT (Westbury, NY). Ultrasensitive Insulin Enzyme-linked Immunosorbent Assay (ELISA) kit was purchased from Mercodia AB (Uppsala, Sweden). Phosphate buffered saline (PBS, 10mM, pH 7.4) was used to rinse electrodes and for electrochemical measurements.

4.2.2 Instrumentation

Cyclic voltammetric and amperometric measurements were performed on CHI 6017E Electrochemical Analyzer (CH Instruments, Austin, TX). Electrochemical impedance spectroscopy (EIS) measurements were performed on Interface 1000 Potentiostat (Gamry Instruments, Warminster, PA). Stepwise characterization of the sensor surface was performed

using Nicolet iS50 Fourier Transform Infrared Spectrometer (ThermoFisher Scientific, Waltham, MA). ELISA estimation of serum insulin measurements were performed using a BioTek Synergy H1 Plate Reader (BioTek Instruments, Winooski, VT).

4.2.3 Preparation of paper electrodes

To design the paper electrodes, Whatman Grade 1 chromatographic paper was cut in 5 cm x 3.2 cm strips. Electrode connections for working and counter electrodes (WE and CE) were prepared by hand drawing graphite ink on the paper substrate. Ag/AgCl ink was used to prepare the reference electrode (RE). The WE comprised a circular base of 5 mm diameter. Each of the electrodes were 3.8 cm x 0.2 cm. A circular hydrophilic region of 1.2 cm diameter encompassing all three electrodes was used as the reaction zone. All other regions of the paper was patterned with wax by first coating it with wax and melting it on a hot plate at 150 ˚C for 1 min to allow the wax to penetrate across the paper substrate allowing the formation of hydrophobic region.

4.2.4 Design of immunosensor surface and electrochemical measurements

Aqueous carboxylated graphene (graphene-COOH, 30 µL of 1 mg mL^{-1}) was drop-casted on the base of the WE. After air drying for approximately 6 h, the electrode was cleaned with water air dried. A mixture of 0.4 M EDC and 0.1 M NHS (30 µL) was added onto the electrode surface for 10 min to activate the COOH terminals of the carboxylated graphene. The electrode was then rinsed with PBS and incubated with 30 µL of amine functionalized insulin aptamers (30 µM in TE buffer, pH 7.5) for 50 min. The activated carboxyl terminals covalently bonded with amine terminals on the aptamers through the formation of the amide bonds. The electrode was rinsed to remove any unbound molecules and incubated with 20 µL of 1% BSA in PBS for 30 min to cover open regions on the electrode as well to deactivate unbound carboxyl terminals. After rinsing the electrode, it was again incubated with 20 µL of 10 mM ethanolamine in PBS for 30 min to cover the electrode region as well as create insulating layer on the electrode surface. At this point, after

rinsing the electrode, the capacitance was measured by EIS for label-free detection. The EIS measurements were performed by connecting the paper electrode to the Gamry potentiostat and scanning frequency from 100,000 – 0.5 Hz while applying 10 mV AC magnitude and 0 V DC potential. The capacitance was monitored at 10 Hz.

Different concentrations of insulin-spiked 10% serum sample (50 μL each) was added onto the electrode surface for 30 min to allow the insulin molecules in the sample to bind to aptamers on the sensor surface. The electrode was rinsed and capacitance was measured again to monitor the change in capacitance after insulin binding.

For amperometric measurements, after incubation with serum insulin sample and rinsing, the electrode surface was further incubated with 50 μL of 1 μg mL^{-1} HRP-labeled polyclonal anti-insulin antibody (Ab_{HRP}) for 30 min. The electrode was then rinsed and connected to a potentiostat. A mixture of 1 mM HQ and 0.5 mM H_2O_2 (200 μL) was added onto the surface and amperometric signals were monitored by applying a potential of -0.1 V.

4.2.5 Immunosensor optimization and characterization

The optimum concentration of aptamer immobilized on the sensor surface was determined using the faradaic impedance spectroscopic measurements. After the immobilization of 30 μL of different concentrations of aptamers on different paper electrodes, they were rinsed and immersed in an aqueous solution containing 0.1 M KCl and 10 mM $Fe(CN)_6^{3-}/Fe(CN)_6^{4-}$. A potential of 150 mV versus a pseudo Ag/AgCl reference electrode was applied at an AC amplitude of 10 mV and was scanned in the frequency range of 100,000 – 0.5 Hz. The resulting impedance curves were fit by the Randles equivalent circuit model to determine the charge transfer resistance (R_{ct}) values.

Each individual modification step on the sensor surface was characterized by FTIR spectroscopy operating in the attenuated total reflection mode using a diamond crystal. The FTIR

spectroscopy allowed the identification of functional vibrations on the stepwise assembly of the immunosensor.

To estimate the number of relative carboxyl groups on the electrode surface after dry coating graphene-COOH solution, the electrodes were first activated by treating them with 0.4 M EDC/0.1 M NHS. Then, 30 µL of 1 mM aminoferrocene in PBS, pH 7.4, was added to the activated surface and incubated for 45 min to allow the immobilization of aminoferrocene on the electrode surface through the formation of amide bonds. After rinsing the electrodes to remove any unbound molecules, cyclic voltammograms were obtained to analyze the electroactive groups on the electrode surface.

4.3 Results and discussion

4.3.1 Aptamer concentration optimization

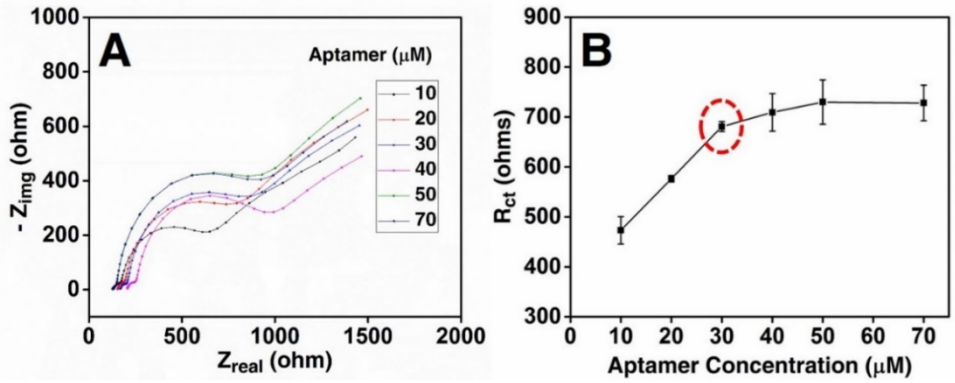

Figure 4.3. (A) Faradaic impedance spectroscopy for different concentrations of aptamer immobilized on graphene-COOH electrode. **(B)** Charge transfer resistance (R_{ct}) obtained by fitting the corresponding curves to Randles equivalent circuit for different concentrations of the insulin aptamer. The red dashed-circle denotes the 30 µM concentration chosen as the optimum aptamer concentration. (N=3 replicates.)

The optimum concentration of immobilized aptamer on the sensor surface was determined through faradaic EIS as illustrated in Figure 4.3. Figure 4.3-A shows the Nyquist plots for different concentrations of aptamer immobilized on separate paper electrodes. These plots were fit in Randles equivalent circuit model to obtain the R_{ct} values. The R_{ct} values corresponds to the diameter of the semi-circle in the Nyquist plots. The plot of R_{ct} versus different concentrations of aptamers (Figure 4.3-B) allowed us to identify the optimum concentration of the insulin aptamers on the sensor surface which was 30 μM. Once this optimum concentration was established, further modifications on the electrode surface were performed by keeping the concentration constant throughout the entire study.

4.3.2 Immunosensor characterization and carboxyl group estimation

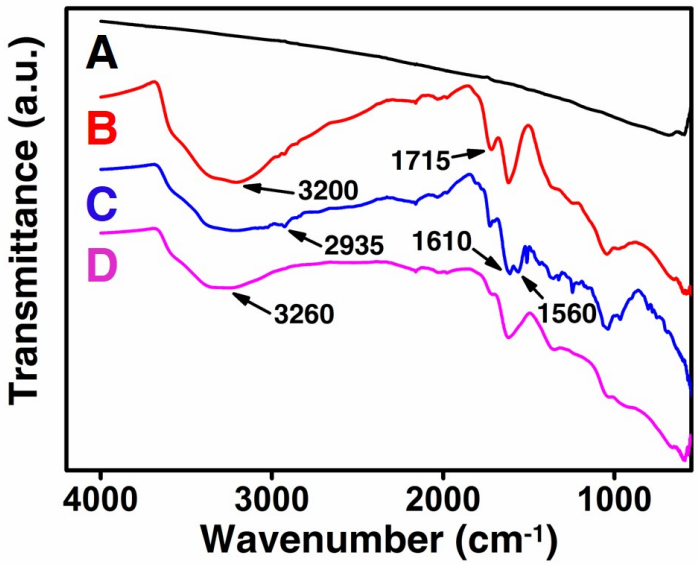

Figure 4.4. FTIR characterization of the stepwise assembly of the immunosensor; **(A)** bare graphite electrode, **(B)** after graphene-COOH coating, **(C)** after aptamer immobilization, and **(D)** after double blocking of the surface and insulin capturing via aptamers.

Figure 4.4 illustrates the stepwise FTIR characterization of the sensor surface after each modification step. The bare graphite electrodes did not show any significant peaks. However,

after graphene-COOH coating, a broad peak was seen at about 3200 cm^{-1} that was attributed to the hydroxyl stretching, and a peak at 1715 cm^{-1} was attributed to C=O stretching. Upon binding of insulin aptamers, amide I and amide II peaks were observed at 1610 and 1560 cm^{-1} respectively, along with N-H stretching at about 3260 cm^{-1}. A peak at about 2935 cm^{-1} was more pronounced and was attributed to heterocyclic bases of the single stranded DNA aptamer. The same peaks remain prominent after double blocking and insulin immobilization step.

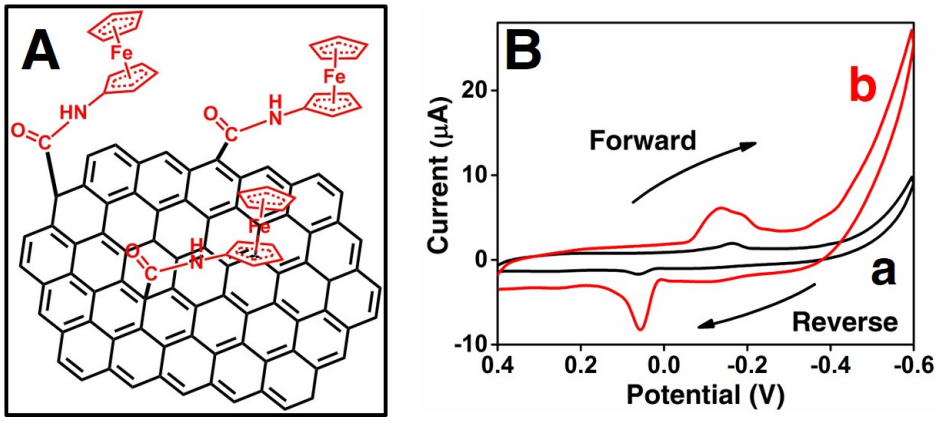

Figure 4.5. (A) Representation of the labeling of carboxylated graphene with aminoferrocene molecules through formation of amide bonds. **(B)** Cyclic voltammograms of **(a)** bare graphite and **(b)** graphene-COOH coated paper-based electrode with covalently attached aminoferrocene in argon-purged PBS, pH 7.4, at 23 ºC at a scan rate of 0.1 V s^{-1}.

Estimation of the relative carboxyl groups on the bare graphite paper-electrode and graphene-COOH coated graphite paper-electrode were determined by cyclic voltammograms of redox active aminoferrocene labels covalently attached to carboxyl terminals through the formation of amide bonds (Figure 4.5-A,B). The integrated peak area correlated to the amount of electroactive aminoferrocene molecules bound to the surface. The oxidation peak area was used to calculate the amount of surface coverage of aminoferrocene molecules using Equation 4.2, which correlated to amount of carboxyl groups on the electrode surface.[101]

$$\Gamma = Q/(nFA) \qquad \text{(Equation 4.2)}$$

Here, Q is the oxidation peak area, n is the number of electron for aminoferrocene oxidation (n = 1), F is Faraday's constant, and A is the area of the working electrode (0.2 cm^2).

The calculated amount of relative carboxyl terminals in bare graphite electrode and graphene-COOH coated graphite electrode were 6.72 ± 0.66 and 50.30 ± 8.94 pmoles cm^{-2} respectively. The graphene coated electrode offered almost 8 times higher number of carboxyl terminals on the electrode surface. This ultimately enables the sensor surface to accommodate higher number of biological recognition elements, which in this case are insulin aptamers.

4.3.3 Impedimetric characterization of the paper-based sensor

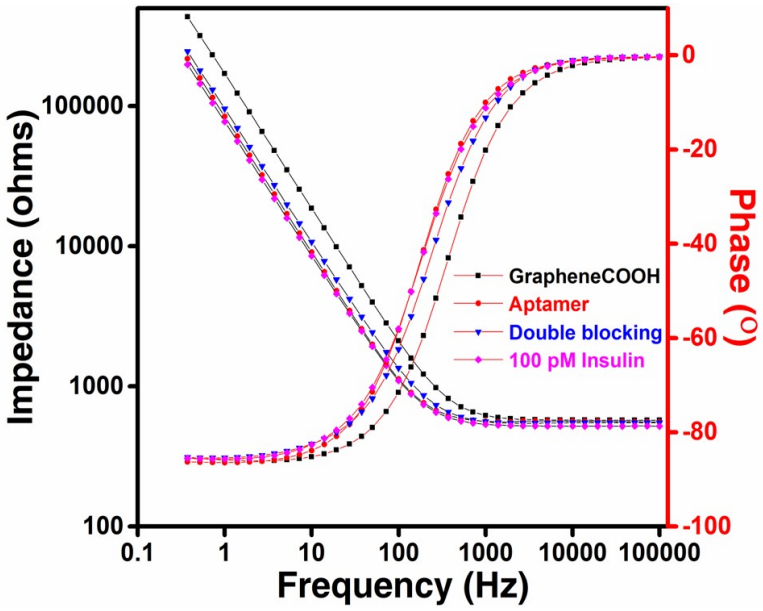

Figure 4.6. Bode plot representing the stepwise assembly of the paper-based capacitive sensor. 100 pM insulin spiked in 10% human serum was used for demonstrating the Bode plot after analyte capturing. EIS was obtained after each modification step by applying 10 mV AC waveform magnitude and scanning from 100,000 – 0.5 Hz.

Figure 4.6 represents the Bode plot for stepwise assembly of molecules on the paper-based electrode. The Bode plot represents the impedance and phase angle change for the stepwise electrode assembly after applying 10 mV AC potential and scanning in the frequency range of 100,000 – 0.5 Hz. The immunosensing electrode behaves as a resistor at higher frequencies as impedance values remains constant given that resistance is independent of frequency. However, as we approach lower frequencies, the sensor starts to behave as a capacitor and the impedance starts to increase with decreasing frequencies. At lower frequencies (< 100 Hz), the immunosensor approaches an ideal capacitor as the phase angle approaches -90º indicating densely packed insulating layer.[32] For monitoring capacitance change before and after the insulin capturing, we chose 10 Hz as the optimum frequency given that it relatively takes less time while still behaving as an ideal capacitor.

4.3.4 Insulin dependent change in capacitance and amperometric signals

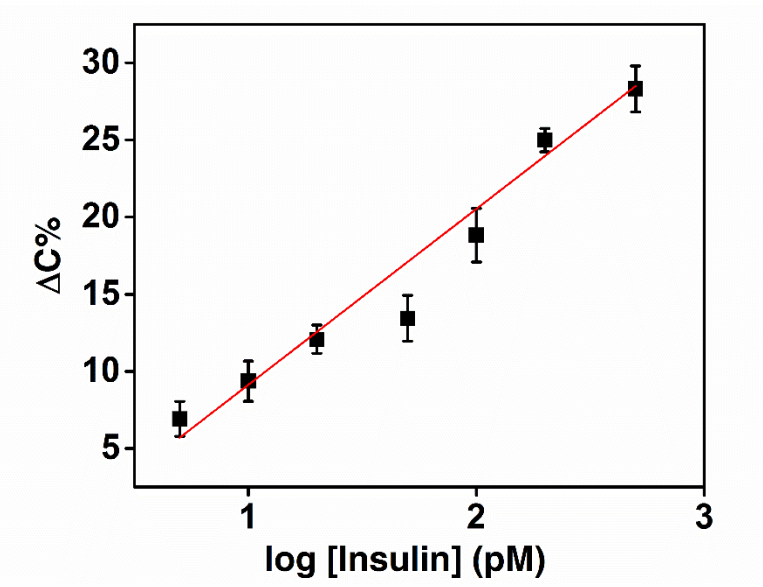

Figure 4.7. Control subtracted capacitance response plot for different concentrations of insulin spiked in 10% serum and immobilized on graphene-COOH surface. The capacitance was monitored at 10 Hz frequency while applying a 10 mV AC potential. (N=3 replicates.)

Figure 4.7 represents the relative change in capacitance against different concentration of insulin spiked in 10% serum samples. The $\Delta C\%$ represents the percentage change in capacitance before and after the immobilization of insulin molecules and is given by Equation 4.3,

$$\Delta C\% = \frac{(C_1 - C_0)}{C_0} X\ 100\% \qquad \text{(Equation 4.3)}$$

Here, C_0 and C_1 represents the capacitance before and after insulin immobilization respectively.

This capacitive sensor exhibited a good dynamic range of 5 – 500 pM and a limit of detection (LOD) of 1.5 pM. These analytical values are clinically significant. Yagati *et al.* proposed a capacitive sensor for detecting insulin molecules where the capacitance decreased with increasing concentration of insulin as opposed to this study.[22] This was attributed to increase in distance with increasing concentration of insulin due to formation of antigen-antibody complexes. However, other studies have mentioned increase in capacitance for increasing antigen-antibody complexes at lower frequencies.[135] Especially in the case of aptamer-antigen complexes, capacitance has found to be increasing owing to increase in dielectric properties due to the formation of aptamer-antigen complexes.[136-138]

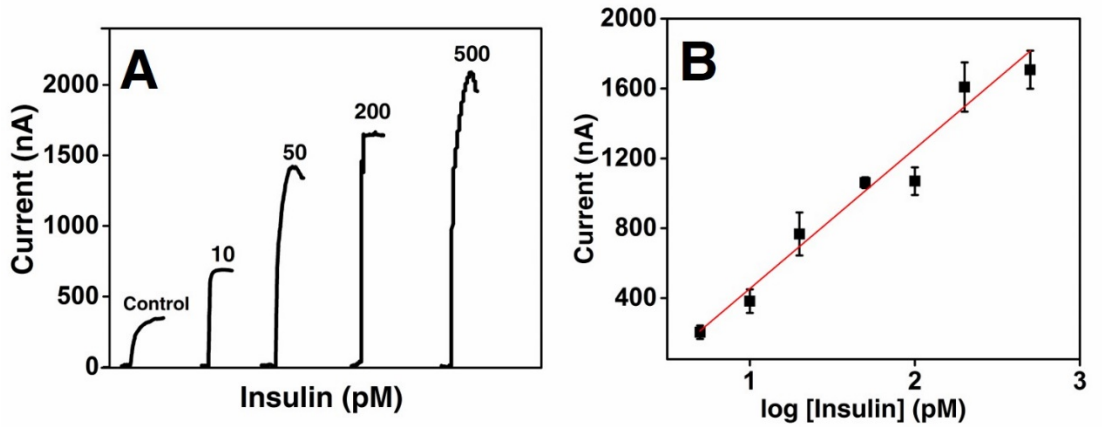

Figure 4.8. (A) Amperometric response curves for different concentrations of insulin spiked in 10% serum samples. **(B)** Control subtracted correlation of current with different concentrations of insulin spiked in serum. (N=3 replicates.)

As mentioned prior, the paper-based immunosensor was further analyzed using amperometry. This was achieved by incubating the sensor surface with HRP-labeled anti-insulin polyclonal antibodies after the insulin incubation. The prepared electrodes were connected to a potentiostat and a 200 µL mixture of 0.1 mM HQ and 0.5 mM H_2O_2 was added to the surface while applying -0.1 V potential, and the current signals were monitored. Thus obtained current signals correlated to the concentration of insulin on sensor surface (Fig. 4.8-A). Figure 4.8-B represents the correspondence of control subtracted current signals to different serum insulin concentration. The analytical parameters of this amperometric immunosensor were comparable to the capacitive sensor. The exhibited dynamic range was 5 – 500 pM and an LOD of 1 pM.

4.3.5 Validation of sensor with insulin ELISA

To assess the clinical applicability of the both paper-based capacitive and amperometric sensors, we analyzed a type 2 diabetes patient serum sample (10% serum) using a commercial ELISA kit as well as with the paper-based immunosensor in both capacitive and amperometric platforms. The diluted patient sample was back calculated to determine the undiluted concentration of the patient sample. The patient sample analysis correlated well across all three immunosensing

techniques. The paper-based assay strategies required less time (capacitive ~ 2.5 h; amperometric ~ 3 h) compared to ELISA technique where the assay time takes ~ 3 h excluding the time spent in manufacturing.

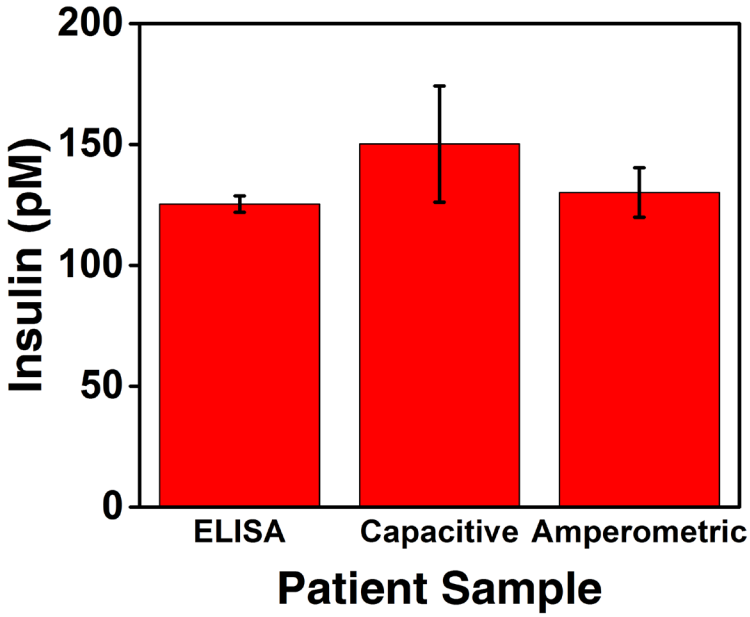

Figure 4.9. Correlation of the paper-based capacitive and amperometric biosensors with commercial insulin ELISA kit for a type 2 diabetes patient sample. (N=3 replicates.)

4.4 Conclusion

The paper-based graphene electrode immunosensor measured serum insulin molecules in both enzyme-amperometric and label-free non-faradaic impedance techniques. Insulin aptamers were able to provide selectivity to capture insulin molecules in 10% serum samples. Amperometric and capacitance detection methods provided comparable results for measuring insulin molecules in clinically relevant levels. Capacitive detection of biomolecules can be performed in less number of steps and thus, less amount of time without the need for expensive enzymatic labels when compared to amperometric technique. However, manual electrode fabrication technique may not

be feasible for large scale production as well may present significant batch-to-batch variations. As a future outlook, we are focusing towards inkjet printing wax and electrodes to minimize above mentioned predicaments. Additionally, minimizing incubation time and sample volume and adapting the sensor system for measuring analytes in whole blood will be the emphasis of the future direction. Nonetheless, paper-based electrodes can be adopted as a cheaper alternative to 3-electrode systems as well as screen printed electrodes when it comes to detecting biomolecules at point-of-care.

CHAPTER V

CONCLUSION AND FUTURE OUTLOOK

Since their inception, glucose biosensors (normal and diabetes related blood glucose concentration is present in several millimolar units) have seen immense success on diabetes management. Recently, insulin detection approaches in biofluids have gained significance for regulating glucose metabolism, and for potential applicability in identification of type 1 (insulin-deficient condition) and type 2 (insulin-resistant condition) diabetic disorders, as well as for use in artificial pancreatic devices. In addition to insulin, other non-glucose molecules (e.g., autoantibodies, receptors, proteins, and other small molecules) are evolving as early predictive biomarkers of diabetes and diabetes related complications. The objective of this dissertation was to advance the current analytical capabilities for detecting insulin and diabetes autoantibodies by novel surface chemistry designs and provide quantitative insights. Simplicity of the sensor design, low-cost label-free paper designs, sensitivity, and clinically required detection limits are some of the unique advantages offered from the collective studies in this dissertation.

In Chapter II, we reported that the combination of π-π stacking of pyrenecarboxylic acid (Py-COOH) over chemically carboxylated multiwall carbon nanotubes (MWNT-COOH) offers superior sensitivity compared to MWNT-COOH alone for serum insulin measurements. Additionally, quantitative details on the relative number of carboxyl groups and protein immobilization were presented for both MWNT-COOH/Py-COOH and MWNT-COOH surfaces.

The results indicated that enhancing the number of carboxylic acid groups on the carbon nanotubes surface enhanced the number of proteins immobilized, thus improving the dynamic range and limit of detection for serum insulin measurements. The approach discussed in the study is broadly applicable for biosensors, drug delivery, and catalytic systems.

Chapter III demonstrated our initial exploration into the islet cell autoantibodies detection as type 1 diabetes predictive biomarker. The study presented surface-plasmon microarray detection of serum glutamic acid decarboxylase 65 autoantibody (GADA) utilizing the antigen GAD-65 as the biorecognition element. The binding events for the antigen-antibody complexes were studied on a carboxylated graphene and mercapto- monolayer surface for assessing analytical parameters among the two surfaces. Additionally, the binding parameters for the autoantibody-antigen complexes were also presented. Carboxylated-graphene modified immunoassembly on a gold surface-plasmon chip compared to self-assembled monolayer surface of mercaptopropionic acid (MPA) provided significantly larger binding affinity, higher sensitivity, and lower detection limits. Estimation of the relative surface carboxyl groups by covalent tagging of aminoferrocene showed that the graphene surface displayed a greater number of carboxyl groups than the MPA surface. X-ray-photoelectron-spectroscopy analysis showed more C−O and C=O functionalities on the graphene-COOH surface than on the MPA surface. The graphene-COOH coating on gold exhibited ~ 5.5-fold enhancement of plasmon signals compared with a similar coating on a plain glass surface. The binding-constant parameters can be useful as a quality-control checkpoint for reproducible and reliable production of large-scale biosensors for clinical bioassays.

In Chapter IV, we demonstrated a paper-based platform for detecting serum insulin molecules as a cheap alternative to standard analytical laboratory techniques. The study reported non-faradaic impedance (label-free technique) for measuring serum insulin in picomolar range and provided analytical comparison of the paper-based biosensor with amperometric (labeled

technique) methods of insulin measurements. Both the techniques provided comparative dynamic range and lower limit of detection and were able to measure clinically relevant serum insulin concentrations. The study presented surface characterizations with quantitative estimation of carboxyl groups on the sensor surface. The study is reported as a low-cost option for detection of biomolecules.

Overall, we demonstrated surface chemistry for detecting biomolecules of significance in diabetes management and prediction with clinical significance. Moving ahead, our objective to enhance the analytical parameters remains the same. Ultimately, we want to design and develop sensors for point-of-care testing capable of measuring analytes directly from undiluted biofluids. Multiplexed detection of biomarkers in a paper-based platform while still detailing on the surface characteristics and the sensors surface robustness and reproducibility is the scope of the future direction.

REFERENCES

1. Hu, F. B.; Satija, A.; Manson, J. E. *JAMA* **2015**, *313*, 2319-2320.

2. World Health Organization. Global report on diabetes. https://www.who.int/diabetes/global report/en/ (accessed June 17, 2019).

3. Centers for Disease Control and Prevention. A Snapshot: Diabetes in the United States. https://www.cdc.gov/diabetes/library/socialmedia/infographics.html (accessed June 17, 2019).

4. American Diabetes Association. *Diabetes Care* **2017**, *40*, S11-S24.

5. Stenström, G.; Gottsäter, A.; Bakhtadze, E.; Berger, B.; Sundkvist, G. *Diabetes* **2005**, *54*, S68-S72.

6. Quianzon, C. C.; Cheikh, I. *J. Community Hosp. Intern. Med. Perspect.* **2012**, *2*, 18701.

7. Clark Jr, L. C.; Lyons, C. *Ann. N. Y. Acad. Sci.* **1962**, *102*, 29-45.

8. Yoo, E.-H.; Lee, S.-Y. *Sensors* **2010**, *10*, 4558-4576.

9. Chen, C.; Xie, Q.; Yang, D.; Xiao, H.; Fu, Y.; Tan, Y.; Yao, S. *RSC Adv.* **2013**, *3*, 4473-4491.

10 Tonyushkina, K.; Nichols, J. H. *J. Diabetes Sci. Technol.* **2009**, *3*, 971-980.

11. Weiss, M.; Steiner, D. F.; Philipson, L. H. *Insulin Biosynthesis, Secretion, Structure, and Structure-Activity Relationships*; MDText.com, Inc., South Dartmouth (MA), 2000.

12. American Diabetes Association. Diagnosing Diabetes and Learning about Prediabetes. http://www.diabetes.org/diabetes-basics/diagnosis/ (accessed June 30, 2019).

13. Freckmann, G.; Hagenlocher, S.; Baumstark, A.; Jendrike, N.; Gillen, R. C.; Rössner, K.; Haug, C. *J. Diabetes Sci. Technol.* **2007**, *1*, 695-703.

14. Muoio, D. M.; Newgard, C. B. *Nat. Rev. Mol. Cell Biol.* **2008**, *9*, 193-205.

15. Weyer, C.; Hanson, R. L.; Tataranni, P. A.; Bogardus, C.; Pratley, R. E. *Diabetes* **2000**, *49*, 2094-2101.

16. Goetz, F. C.; French, L. R.; Thomas, W.; Gingerich, R. L.; Clements, J. P. *Metabolism* **1995**, *44,* 1371-1376.

17. Singh, V.; Krishnan, S. *Analyst* **2014**, *139*, 724-728.

18. Singh, V.; Krishnan, S. *Anal. Chem.* **2015**, *87*, 2648-2654.

19. Singh, V.; Rodenbaugh, C.; Krishnan, S. *ACS Sens.* **2016**, *1*, 437-443.

20. Singh, V.; Nerimetla, R.; Yang, M.; Krishnan, S. *ACS Sens.* **2017**, *2*, 909-915.

21. Li, T.; Liu, Z.; Wang, L.; Guo, Y. *RSC Adv.* **2016**, *6*, 30732-30738.

22. Yagati, A. K.; Park, J.; Cho, S. *Sensors (Basel, Switzerland)* **2016**, *16*, 109.

23. Amouzadeh Tabrizi, M.; Shamsipur, M.; Saber, R.; Sarkar, S.; Besharati, M. *Microchim. Acta* **2017**, *185*, 59.

24. E. Bonifacio, *Diabetes Care*, 2015, **38**, 989-996.

25. Ziegler, A. G.; Rewers, M.; Simell, O.; Simell, T.; Lempainen, J.; Steck, A.; Winkler, C.; Ilonen, J.; Veijola, R.; Knip, M.; Bonifacio, E.; Eisenbarth, G. S. *JAMA* **2013**, *309*, 2473-2479.

26. Falorni, A.; Örtqvist, E.; Persson, B.; Lernmark, Å. *J. Immunol. Methods* **1995**, *186*, 89-99.

27. Walikonis, J. E.; Lennon, V. A. *Mayo Clin. Proc.* **1998**, *73*, 1161-1166.

28. Zhang, B.; Kumar, R. B.; Dai, H.; Feldman, B. J. *Nat. Med.* **2014**, *20*, 948-953.

29. Zhao, Z.; Miao, D.; Michels, A.; Steck, A.; Dong, F.; Rewers, M.; Yu, L. *J. Immunol. Methods* **2016**, *430*, 28-32.

30. Amoroso, M.; Achenbach, P.; Powell, M.; Coles, R.; Chlebowska, M.; Carr, L.; Furmaniak, J.; Scholz, M.; Bonifacio, E.; Ziegler, A.-G.; Rees Smith, B. *Clin. Chim. Acta* **2016**, *462*, 60-64.

31. Katz, E.; Willner, I. *Electroanalysis* **2003**, *15*, 913-947.

32. Sharma, R.; Deacon, S. E.; Nowak, D.; George, S. E.; Szymonik, M. P.; Tang, A. A. S.; Tomlinson, D. C.; Davies, A. G.; McPherson, M. J.; Wälti, C. *Biosens. Bioelectron.* **2016**, *80*, 607-613.

33. Li, M.; Cushing, S. K.; Wu, N. *Analyst* **2015**, *140*, 386-406.

34. Mariani, S.; Minunni, M. *Anal. Bioanal. Chem.* **2014**, *406*, 2303-2323.

35. Krishnan, S.; Armstrong, F. A. *Chem. Sci.* **2012**, *3*, 1015-1023.

36. Yu, X.; Munge, B.; Patel, V.; Jensen, G.; Bhirde, A.; Gong, J. D.; Kim, S. N.; Gillespie, J.; Gutkind, J. S.; Papadimitrakopoulos, F.; Rusling, J. F. *J. Am. Chem. Soc.* **2006**, *128*, 11199-11205.

37. Gong, K.; Du, F.; Xia, Z.; Durstock, M.; Dai, L. *Science* **2009**, *323*, 760-764.

38. Reuillard, B.; Gentil, S.; Carriere, M.; Le Goff, A.; Cosnier, S. *Chem. Sci.* **2015**, *6*, 5139-5143.

39. Meredith, M. T.; Minson, M.; Hickey, D.; Artyushkova, K.; Glatzhofer, D. T.; Minteer, S. D. *ACS Catal.* **2011**, *1*, 1683-1690.

40. Byers, J. C.; Güell, A. G.; Unwin, P. R. *J. Am. Chem. Soc.* **2014**, *136*, 11252-11255.

41. Zou, X.; Huang, X.; Goswami, A.; Silva, R.; Sathe, B. R.; Mikmeková, E.; Asefa, T. *Angew. Chem. Int. Ed.* **2014**, *53*, 4372-4376.

42. Tran, P. D.; Le Goff, A.; Heidkamp, J.; Jousselme, B.; Guillet, N.; Palacin, S.; Dau, H.; Fontecave, M.; Artero, V. *Angew. Chem. Int. Ed.* **2011**, *50*, 1371-1374.

43. Yan, Y.; Miao, J.; Yang, Z.; Xiao, F.-X.; Yang, H. B.; Liu, B.; Yang, Y. *Chem. Soc. Rev.* **2015**, *44*, 3295-3346.

44. Zhang, J.; Dai, L.; Xia, Z. *Sci. Adv.* **2015**, *1*, e1500564.

45. Wang, Z.; Dai, Z. *Nanoscale* **2015**, *7*, 6420-6431.

46. Tiwari, J. N.; Vij, V.; Kemp, K. C.; Kim, K. S. *ACS Nano* **2016**, *10*, 46-80.

47. Lojou, E. *Electrochim. Acta* **2011**, *56*, 10385-10397.

48. Wang, J. *Electroanal.* **2005**, *17*, 7-14.

49. Wang, D.-Y.; Gong, M.; Chou, H.-L.; Pan, C.-J.; Chen, H.-A.; Wu, Y.; Lin, M.-C.; Guan, M.; Yang, J.; Chen, C.-W.; Wang, Y.-L.; Hwang, B.-J.; Chen, C.-C.; Dai, H. *J. Am. Chem. Soc.* **2015**, *137*, 1587-1592.

50. Huang, S.; Liang, C.; Chen, Y.-J. *Ind. Eng. Chem. Res.* **2016**, *55*, 6060-6068.

51. Li, H.; Chen, Q.; Han, B.-H. *New J. Chem.* **2016**, *40*, 3300-3307.

52. Rabti, A.; Raouafi, N.; Merkoçi, A. *Carbon* **2016**, *108*, 481-514.

53. Chen, R. J.; Zhang, Y.; Wang, D.; Dai, H. *J. Am. Chem. Soc.* **2001**, *123*, 3838-3839.

54. Walgama, C.; Means, N.; Materer, N. F.; Krishnan, S. *Phys. Chem. Chem. Phys.* **2015**, *17*, 4025-4028.

55. Krishnan, S.; Mani, V.; Wasalathanthri, D.; Kumar, C. V.; Rusling, J. F. *Angew. Chem. Int. Ed.* **2011**, *50*, 1175-1178.

56. Singh, V.; Rodenbaugh, C.; Krishnan, S. *ACS Sensors* **2016**, *1*, 437-443.

57. Zhang, Y.; Yuan, S.; Zhou, W.; Xu, J.; Li, Y. *J. Nanosci. Nanotechnol.* **2007**, *7*, 2366-2375.

58. Prasad, K. S.; Walgama, C.; Krishnan, S. *RSC Adv.* **2015**, *5*, 11845-11849.

59. Karachevtsev, V.A.; Stepanian, S. G.; Glamazda, A. Y.; Karachevtsev, M. V.; Eremenko, V. V.; Lytvyn, O. S.; Adamowicz, L. *J. Phys. Chem. C* **2011**, *115*, 21072-21082.

60. Masheter, A. T.; Xiao, L.; Wildgoose, G. G.; Crossley, A.; Jones, J. H.; Compton, R. G. *J. Mater. Chem.* **2007**, *17*, 3515-3524.

61. Armbruster, D. A.; Pry, T. *Clin. Biochem. Rev.* **2008**, *29*, S49-S52.

62. Walgama, C.; Nerimetla, R.; Materer, N. F.; Schildkraut, D.; Elman, J. F.; Krishnan, S. *Anal. Chem.* **2015**, *87*, 4712-4718.

63. Pihoker, C.; Gilliam, L. K.; Hampe, C. S.; Lernmark, Å. *Diabetes* **2005**, *54*, S52-S61.

64. von Herrath, M.; Sanda, S.; Herold, K. *Nat. Rev. Immunol.* **2007**, *7*, 988-994.

65. Gan, M. J.; Albanese-O'Neill, A.; Haller, M. J. *Current Problems in Pediatric and Adolescent Health Care* **2012**, *42*, 269-291.

66. Atkinson, M. A.; Eisenbarth, G. S. *The Lancet* **2001**, *358*, 221-229.

67. Åkerblom, H. K.; Vaarala, O.; Hyöty, H.; Ilonen, J.; Knip, M. *Am. J. Med. Genet.* **2002**, *115*, 18-29.

68. Ziegler, A.-G.; Nepom, G. T. *Immunity* **2010**, *32*, 468-478.

69. Bonifacio, E. *Diabetes Care* **2015**, *38*, 989-996.

70. Verge, C. F.; Gianani, R.; Kawasaki, E.; Yu, L.; Pietropaolo, M.; Chase, H. P.; Eisenbarth, G. S.; Jackson, R. A. *Diabetes* **1996,** *45*, 926.

71. Heding, L. G. *Diabetologia* **1975**, *11*, 541-548.

72. Andersen, L.; Dinesen, B.; Jorgensen, P. N.; Poulsen, F.; Roder, M. E. *Clin. Chem.* **1993**, *39*, 578-582.

73. Forest, J. C.; Masse, J.; Lane, A. *Clin. Biochem.* **1998**, *31*, 81-88.

74. Miao, D.; Guyer, K. M.; Dong, F.; Jiang, L.; Steck, A. K.; Rewers, M.; Eisenbarth, G. S.; Yu, L. *Diabetes* **2013**, *62*, 4174-4178.

75. Lee, J. W.; Sim, S. J.; Cho, S. M.; Lee, J. *Biosens. Bioelectron.* **2005**, *20*, 1422-1427.

76. Choi, S. H.; Lee, J. W.; Sim, S. J. *Biosens. Bioelectron.* **2005**, *21*, 378-383.

77. Cao, C.; Sim, S. J. *Biosens. Bioelectron.* **2007**, *22*, 1874-1880.

78. Nguyen, H. H.; Park, J.; Kang, S.; Kim, M. *Sensors* **2015**, *15*, 10481-10510.

79. Bonaccorso, F.; Sun, Z.; Hasan, T.; Ferrari, A. C. *Nat. Photon.* **2010**, *4*, 611-622.

80. Chiu, N.-F.; Huang, T.-Y.; Lai, H.-C.; Liu, K.-C. *Nanoscale Res. Lett.* **2014**, *9*, 445-451.

81. Lee, H.; Choi, T. K.; Lee, Y. B.; Cho, H. R.; Ghaffari, R.; Wang, L.; Choi, H. J.; Chung, T. D.; Lu, N.; Hyeon, T.; Choi, S. H.; Kim, D.-H. *Nat. Nano.* **2016**, *11*, 566-572.

82. Patil, A. V.; Fernandes, F. B.; Bueno, P. R.; Davis, J. J. *Bioanalysis* **2015**, *7*, 725-742.

83. Yang, W.; Ratinac, K. R.; Ringer, S. P.; Thordarson, P.; Gooding, J. J.; Braet, F. *Angew. Chem. Int. Ed.* **2010**, *49*, 2114-2138.

84. Ma, H.; Wu, D.; Cui, Z.; Li, Y.; Zhang, Y.; Du, B.; Wei, Q. *Anal. Lett.* **2013**, *46*, 1-17.

85. Zeng, S.; Baillargeat, D.; Ho, H.-P.; Yong, K.-T. *Chem. Soc. Rev.* **2014**, *43*, 3426-3452.

86. He, L.; Pagneux, Q.; Larroulet, I.; Serrano, A. Y.; Pesquera, A.; Zurutuza, A.; Mandler, D.; Boukherroub, R.; Szunerits, S. *Biosens. Bioelectron.* **2017**, *89*, 606-611.

87. Zagorodko, O.; Spadavecchia, J.; Serrano, A. Y.; Larroulet, I.; Pesquera, A.; Zurutuza, A.; Boukherroub, R.; Szunerits, S. *Anal. Chem.* **2014**, *86*, 11211-11216.

88. Geim, A. K. *Science* **2009**, *324*, 1530-1534.

89. Zhu, Y.; Murali, S.; Cai, W.; Li, X.; Suk, J. W.; Potts, J. R.; Ruoff, R. S. *Adv. Mater.* **2010**, *22*, 3906-3924.

90. Schedin, F.; Lidorikis, E.; Lombardo, A.; Kravets, V. G.; Geim, A. K.; Grigorenko, A. N.; Novoselov, K. S.; Ferrari, A. C. *ACS Nano* **2010**, *4*, 5617-5626.

91. Grigorenko, A. N.; Polini, M.; Novoselov, K. S. *Nat. Photon.* **2012**, *6*, 749-758.

92. Wang, H.; Shi, L.; Yan, T.; Zhang, J.; Zhong, Q.; Zhang, D. *J. Mater. Chem. A.* **2014**, *2*, 4739-4750.

93. Wu, H.; Zhao, W. F.; Hu, H. W.; Chen, G. H. *J. Mater. Chem.* **2011**, *21*, 8626-8632.

94. Wu, N.; She, X.; Yang, D.; Wu, X.; Su, F.; Chen, Y. *J. Mater. Chem*. **2012**, *22*, 17254-17261.

95. Ding, W.; Cai, J.; Yu, Z.; Wang, Q.; Xu, Z.; Wang, Z.; Gao, C. *J. Mater. Chem. A*. **2015**, *3*, 20118-20126.

96. Falahati-Pour, S. K.; Lotfi, A. S.; Ahmadian, G.; Baghizadeh, A. *J. Appl. Microbiol*. **2015**, *118*, 976-988.

97. Song, X.; Wang, L.; Tang, C. Y.; Wang, Z.; Gao, C. *Desalination* **2015**, *369*, 1-9.

98. Liao, T.; Yuan, F.; Yu, H.; Li, Z. *Anal. Methods* **2016**, *8*, 1577-1585.

99. Stankovich, S.; Dikin, D. A.; Piner, R. D.; Kohlhaas, K. A.; Kleinhammes, A.; Jia, Y.; Wu, Y.; Nguyen, S. T.; Ruoff, R. S. *Carbon* **2007**, *45*, 1558-1565.

100. Park, S.; An, J.; Piner, R. D.; Jung, I.; Yang, D.; Velamakanni, A.; Nguyen, S. T.; Ruoff, R. S.. *Chem. Mater.* **2008**, *20*, 6592-6594.

101. Booth, M.A.; Kannappan, K.; Hosseini, A.; Partridge, A. *Langmuir* **2015**, *31*, 8033-8041.

102. Santos. E. J; Kaxiras, E. *Nano. Lett.* **2013**, *13*, 898-902.

103. Walgama, C.; Al Mubarak, Z. H.; Zhang, B.; Akinwale, M.; Pathiranage, A.; Deng, J.; Berlin, K. D.; Benbrook, D. M.; Krishnan, S. *Anal. Chem.* **2016**, *88*, 3130-3135.

104. Nogues, C.; Leh, H.; Langendorf, C. G.; Law, R. H. P.; Buckle, A. M.; Buckle, M. *PLoS ONE* **2010**, *5*, e12152.

105. Mani, V.; Wasalathanthri, D. P.; Joshi, A. A.; Kumar, C. V.; Rusling, J. F. *Anal. Chem.* **2012**, *84*, 10485-10491.

106. *Clinical Pharmacology & Therapeutics* **2001**, *69*, 89-95.

107. Svenningsson, P.; Westman, E.; Ballard, C.; Aarsland, D. *Lancet Neurol.* **2012**, *11*, 697-707.

108. Molinuevo, J. L.; Blennow, K.; Dubois, B.; Engelborghs, S.; Lewczuk, P.; Perret-Liaudet, A.; Teunissen, C. E.; Parnetti, L. *Alzheimers Dement.* **2014**, *10*, 808-817.

109. Chen, X.; Ba, Y.; Ma, L.; Cai, X.; Yin, Y.; Wang, K.; Guo, J.; Zhang, Y.; Chen, J.; Guo, X.; Li, Q. *Cell Res.* **2008,** *18*, 997-1006.

110. Sattar, N. *Diabetic Med.* **2012**, *29*, 5-13.

111. Füzéry, A. K.; Levin, J.; Chan, M. M.; Chan, D. W. *Clinical proteomics* **2013**, *10*, 13.

112. Wu, L.; Qu, X. *Chem. Soc. Rev.* **2015**, *44*, 2963-2997.

113. Topkaya, S. N.; Azimzadeh, M.; Ozsoz, M. *Electroanalysis* **2016**, *28*, 1402-1419.

114. Hua, Q. *Protein Cell* **2010**, *1*, 537-551.

115. Wang, Y.; Gao, D.; Zhang, P.; Gong, P.; Chen, C.; Gao, G.; Cai, L. *Chem. Commun.* **2014**, *50*, 811-813.

116. Sun, H.; Wu, S.; Zhou, X.; Zhao, M.; Wu, H.; Luo, R.; Ding, S. *Microchim. Acta* **2018**, *186*, 6.

117. Luo, X.; Xu, M.; Freeman, C.; James, T.; Davis, J. J. *Anal. Chem.* **2013**, *85*, 4129-4134.

118. Rafiee, B.; Fakhari, A. R. *Biosens. Bioelectron.* **2013**, *46*, 130-135.

119. Kosack, C. S.; Page, A.-L.; Klatser, P. R. *Bull. World Health Organ.* **2017**, *95*, 639-645.

120. Berggren, C.; Bjarnason, B.; Johansson, G. *Electroanalysis* **2001**, *13*, 173-180.

121. Pumera, M. *Chem. Soc. Rev.* **2010**, *39*, 4146-4157.

122. Ambrosi, A.; Chua, C. K.; Bonanni, A.; Pumera, M. *Chem. Rev.* **2014**, *114*, 7150-7188.

123. Pumera, M.; Ambrosi, A.; Bonanni, A.; Chng, E. L. K.; Poh, H. L. *TrAC Trends Anal. Chem.* **2010**, *29*, 954-965.

124. Guo, Z.; Hao, T.; Du, S.; Chen, B.; Wang, Z.; Li, X.; Wang, S. *Biosens. Bioelectron.* **2013**, *44*, 101-107.

125. Singh, M.; Holzinger, M.; Tabrizian, M.; Winters, S.; Berner, N. C.; Cosnier, S.; Duesberg, G. S. *J. Am. Chem. Soc.* **2015**, *137*, 2800-2803.

126. Raccichini, R.; Varzi, A.; Passerini, S.; Scrosati, B. *Nat. Mater.* **2015**, *14*, 271-279.

127. Premaratne, G.; Niroula, J.; Patel, M. K.; Zhong, W.; Suib, S. L.; Kalkan, A. K.; Krishnan, S. *Anal. Chem.* **2018**, *90*, 12456-12463.

128. Ruscito, A.; DeRosa, M. C. *Front. Chem.* **2016**, *4*, 14.

129. Jalalian, S. H.; Karimabadi, N.; Ramezani, M.; Abnous, K.; Taghdisi, S. M. *Trends Food Sci. Technol.* **2018**, *73*, 45-57.

130. Pang, S.; He, L. *Anal. Methods* **2016**, *8*, 1602-1608.

131. Patel, D. J. *Curr. Opin. Chem. Biol*. **1997**, *1*, 32-46.

132. Patel, D. J.; Suri, A. K.; Jiang, F.; Jiang, L. C.; Fan, P.; Kumar, R. A.; Nonin, S. *J. Mol. Biol*. **1997**, *272*, 645-664.

133. Hermann, T.; Patel, D. J. *Science* **2000**, *287*, 820-825.

134. Niroula, J.; Premaratne, G.; Ali Shojaee, S.; Lucca, D. A.; Krishnan, S. *Chem. Commun.* **2016**, *52*, 13039-13042.

135. de Vasconcelos, E. A.; Peres, N. G.; Pereira, C. O.; da Silva, V. L.; da Silva, E. F.; Dutra, R. F. *Biosens. Bioelectron.* **2009**, *25*, 870-876.

136. Qureshi, A.; Gurbuz, Y.; Kallempudi, S.; Niazi, J. H. *Phys. Chem. Chem. Phys.* **2010**, *12*, 9176-9182.

137. Qureshi, A.; Gurbuz, Y.; Niazi, J. H. *Sens. Actuators B Chem.* **2015**, *220*, 1145-1151.

138. Jo, N.; Kim, B.; Lee, S.-M.; Oh, J.; Park, I. H.; Jin Lim, K.; Shin, J.-S.; Yoo, K.-H. *Biosens. Bioelectron.* **2018**, *102*, 164-170.

VITA

Jinesh Niroula

Candidate for the Degree of

Doctor of Philosophy

Dissertation: QUANTITATIVE NANO-SURFACE CHEMISTRY FOR DIABETES SERUM BIOMARKER ASSAYS

Major Field: Chemistry

Biographical:

Education:

Completed the requirements for the Doctor of Philosophy in Chemistry at Oklahoma State University, Stillwater, Oklahoma in July, 2019.

Completed the requirements for the Bachelor of Science in Chemistry at Cameron University, Lawton, Oklahoma in 2012.

Experience:

Graduate Teaching and Research Assistant, Oklahoma State University (2014 - 2019).
Research: Electrochemical and Surface Plasmon Biosensors/Arrays

Laboratory Technician, SOS Employment Group, Well Services Division, West-Texas, Schlumberger Tech-Corp., USA (2013).

Tutor / Head Tutor, Upward Bound and Open Doors, and Department of Mathematics, Cameron University (2008-2012).

Professional Memberships:

Oklahoma Chapter of the Electrochemical Society (2017)
Phi Lambda Upsilon, Honorary Chemical Society (2017)